PANCHROMATIC OBSERVATIONS AND MODELING OF THE HV TAU C EDGE-ON DISK

2010 ApJ 712 112

(http://iopscience.iop.org/0004-637X/712/1/112)

The Astrophysical Journal, 712:112–129, 2010 March 20 doi:10.1088/0004-637X/712/1/112

PANCHROMATIC OBSERVATIONS AND MODELING OF THE HV TAU C EDGE-ON DISK*

G. Duchêne[1,2], C. McCabe[3], C. Pinte[2,4], K. R. Stapelfeldt[5], F. Ménard[2], G. Duvert[2], A. M. Ghez[6], H. L. Maness[1], H. Bouy[7], D. Barrado y Navascués[8], M. Morales-Calderón[8], S. Wolf[9], D. L. Padgett[10], T. Y. Brooke[10], and A. Noriega-Crespo[10]

[1] Astronomy Department, University of California, Berkeley, CA 94720-3411, USA; gduchene@astro.berkeley.edu
[2] Université Joseph Fourier - Grenoble 1/CNRS, Laboratoire d'Astrophysique de Grenoble (LAOG) UMR 5571, BP 53, 38041 Grenoble Cedex 09, France
[3] IPAC, MS 220-6, California Institute of Technology, Pasadena, CA 91125, USA
[4] School of Physics, University of Exeter, Stocker Road, Exeter EX4 4QL, UK
[5] JPL, MS 183-900, California Institute of Technology, Pasadena, CA 91109-8099, USA
[6] Division of Astronomy and Astrophysics, UCLA, Box 951547, Los Angeles, CA 90095-1562, USA
[7] Instituto de Astrofisica de Canarias, C/Via Lactea s/n, 38200 - La Laguna, Tenerife, Spain
[8] Laboratorio de Astrofisica Estelar y Exoplanetas (LAEX-CAB, INTA-CSIC), P.O. Box 78, 28691 Villanueva de la Cañada (Madrid), Spain
[9] Christian-Albrechts-Universität zu Kiel, Institut für Theoretische Physik und Astrophysik, Leibnizstr. 15, 24098 Kiel, Germany
[10] SSC, MS 220-6, California Institute of Technology, Pasadena, CA 91125, USA
Received 2009 July 6; accepted 2009 November 19; published 2010 February 25

ABSTRACT

We present new high spatial resolution ($\lesssim$0.″1) 1–5 μm adaptive optics images, interferometric 1.3 mm continuum and ^{12}CO 2–1 maps, and 350 μm, 2.8 and 3.3 mm fluxes measurements of the HV Tau system. Our adaptive optics images unambiguously demonstrate that HV Tau AB–C is a common proper motion pair. They further reveal an unusually slow orbital motion within the tight HV Tau AB pair that suggests a highly eccentric orbit and/or a large deprojected physical separation. Scattered light images of the HV Tau C edge-on protoplanetary disk suggest that the anisotropy of the dust scattering phase function is almost independent of wavelength from 0.8 to 5 μm, whereas the dust opacity decreases significantly over the same range. The images further reveal a marked lateral asymmetry in the disk that does not vary over a timescale of two years. We further detect a radial velocity gradient in the disk in our ^{12}CO map that lies along the same position angle as the elongation of the continuum emission, which is consistent with Keplerian rotation around a 0.5–1 $M_{\odot}$ central star, suggesting that it could be the most massive component in the triple system. To obtain a global representation of the HV Tau C disk, we search for a model that self-consistently reproduces observations of the disk from the visible regime up to millimeter wavelengths. We use a powerful radiative transfer model to compute synthetic disk observations and use a Bayesian inference method to extract constraints on the disk properties. Each individual image, as well as the spectral energy distribution, of HV Tau C can be well reproduced by our models with fully mixed dust provided grain growth has already produced larger-than-interstellar dust grains. However, no single model can satisfactorily simultaneously account for all observations. We suggest that future attempts to model this source include more complex dust properties and possibly vertical stratification. While both grain growth and stratification have already been suggested in many disks, only a panchromatic analysis, such as presented here, can provide a complete picture of the structure of a disk, a necessary step toward quantitatively testing the predictions of numerical models of disk evolution.

Key words: planetary systems – protoplanetary disks – stars: individual (HV Tau) – stars: pre-main sequence

Online-only material: color figures

1. INTRODUCTION

Circumstellar disks are an ubiquitous outcome of the stellar formation process and they are believed to be the birth place of planetary systems. The growth of dust particles toward planetesimal sizes along with their vertical settling due to gas drag are processes that are believed to be the first steps toward planet formation. Hydrodynamical models have shown that these processes can be efficient early in the disk evolution (e.g., Weidenschilling 1997; Dullemond & Dominik 2004; Barrière-Fouchet et al. 2005). To test these models, it is necessary to obtain an observation-based description of the structure and dust content of protoplanetary disks as a function of the age of the system and other relevant parameters (e.g., stellar mass).

The dust component of protoplanetary disks has long been studied via its thermal emission from near-infrared to millimeter wavelengths which is frequently associated with low-mass pre-main-sequence T Tauri stars (Kenyon & Hartmann 1987; Bertout et al. 1988; Strom et al. 1989; Beckwith et al. 1990). Both grain growth and dust settling can alter the overall shape of the spectral energy distribution (SED) of a T Tauri star (D'Alessio et al. 2001, 2006; Dullemond & Dominik 2004). Indeed, several studies that analyzed (elements of) the SED of young stars have concluded that both grain growth and settling is occurring in protoplanetary disks (e.g., Beckwith & Sargent 1991; Mannings & Emerson 1994; Furlan et al. 2006; Kessler-Silacci et al. 2006; Rodmann et al. 2006; Natta et al. 2007, and references therein). Unfortunately, such studies suffer from the absence of spatial information inherent to photometric measurements and the high optical thickness of disks in the near- to mid-infrared regime. As a result, comparing an object's SED to radiative transfer models leaves many ambiguities (Chiang et al. 2001). For instance, the inferred total dust mass and the maximum size of the dust grains are inversely correlated because of the dependency of dust opacity on grain size. In addition, most

* Data presented in this study were obtained during the course of ESO program 70.C-0565 and IRAM program O048.

of these studies, which focus on a single type of observations (e.g., millimeter fluxes, silicate emission feature), only probe a limited region of the disk and a small fraction of the entire grain size distribution.

To solve for the ambiguities inherent to SED studies, it is critical to obtain spatially resolved observations. Such observations include thermal emission mapping with (sub)millimeter interferometers (e.g., Keene & Masson 1990; Simon et al. 1992; Lay et al. 1994; Dutrey et al. 1996; Andrews & Williams 2007) and scattered light imaging with optical and near-infrared high-resolution instruments (e.g., Burrows et al. 1996; Roddier et al. 1996; Stapelfeldt et al. 1998). Disks are generally optically thin at long wavelengths, so the former type of observations can probe the entire disk structure. Furthermore, they are very sensitive to the presence of millimeter-sized particles. On the other hand, scattered light images, which only probe dust grains at the disk surface, are very sensitive to the size distribution of micronic grains especially when images at multiple wavelengths are analyzed simultaneously (Watson et al. 2007, and references therein). Both types of observations have already yielded important pieces of evidence supporting both grain growth and dust settling in disks (e.g., Duchêne et al. 2003, 2004; Watson & Stapelfeldt 2004).

While grain growth and settling appear to occur in protoplanetary disks, detailed *quantitative* tests of hydrodynamical models can only be achieved with a detailed view of the entire structure of a disk. This can only be obtained via a multi-technique, panchromatic approach. Unfortunately, observational and computational limitations have so far limited the number of objects for which such an analysis could be conducted to a handful. The most notable examples are the studies of the "Butterfly Star" (Wolf et al. 2003), IM Lup (Pinte et al. 2008), and IRAS 04158+2805 (Glauser et al. 2008). In the former two cases, these studies have unambiguously shown that the dust population is stratified, possibly indicating that dust settling is already occurring. Increasing the number of disks studied in such detail is necessary to disentangle individual peculiarities from genuine trends associated with disk evolution.

HV Tau is a triple system located in the Taurus star-forming region. It consists of a 550 AU wide pair whose optically brightest component is itself a tight (10 AU) visual binary (Simon et al. 1996). Spectroscopic and photometric measurements revealed that this subsystem does not currently experience accretion nor does it show infrared excess. They further establish an age of about 2 Myr for the system (White & Ghez 2001). The third component of the system, HV Tau C, is much fainter yet bluer than HV Tau AB. While Magazzu & Martin (1994) first thought that this source was a Herbig–Haro object, Woitas & Leinert (1998) later proposed that HV Tau C is a normal M0 T Tauri star surrounded by an opaque edge-on disk similar to that found in HH 30 by Burrows et al. (1996). Subsequent high-resolution imaging confirmed this hypothesis (Monin & Bouvier 2000). Stapelfeldt et al. (2003) produced the first model of high-resolution 0.8 and 2.2 μm scattered light images of HV Tau C, finding that dust properties similar to those of interstellar dust grains can account for these images. Their 0.8 μm image also revealed the presence of a roughly spherical envelope, producing a symmetric halo that is more extended than the disk itself, that is likely the remnant of the core from which the system was formed.

As a consequence of their particular viewing geometry, edge-on protoplanetary disks offer a unique opportunity to determine their geometry and dust content. As such, they may be the best candidates to study vertical stratification in protoplanetary disks. They also are comparatively easy targets for high angular resolution instruments since the contrast requirement is strongly relaxed. On the other hand, they are challenging from the modeling point of view because of the difficulty of accurately solving for radiative transfer including anisotropic scattering in high optical depth regions. Previous modeling efforts of edge-on protoplanetary disks have therefore focused on interpreting one type of observation at a time (Burrows et al. 1996; Stapelfeldt et al. 1998, 2003; Cotera et al. 2001; Wood et al. 2002; Watson & Stapelfeldt 2004). While these studies proved highly valuable to constrain some of the disk properties, no self-consistent model was used to model all data at once, leaving unexplained contradictions.

Our objective in this work is to perform a global analysis of the HV Tau C disk, combining scattered light images, millimeter interferometric data, and the overall SED into a single fit. We present a series of new observations of the system in Section 2 and discuss our empirical results in Section 3. In Section 4, we present radiative transfer models of the HV Tau C disk and discuss their implications in Section 5. Section 6 summarizes our results.

2. OBSERVATIONS

2.1. Adaptive Optics Near-infrared Imaging

2.1.1. 1–2 μm Imaging

On 2002 November 24, we observed HV Tau using the NAOS adaptive optics system and the CONICA instrument (Lenzen et al. 2003; Rousset et al. 2003) installed on the Yepun 8.2 m Unit Telescope at ESO's Very Large Telescope, as part of the NAOS Guaranteed Time Observing program. We used the 0.″0133 pixel scale for the J ($\lambda_0 = 1.27$ μm, $\Delta\lambda = 0.25$ μm) and H ($\lambda_0 = 1.66$ μm, $\Delta\lambda = 0.33$ μm) images and the 0.″0270 plate scale for the K_s ($\lambda_0 = 2.18$ μm, $\Delta\lambda = 0.35$ μm) images. HV Tau AB, a $m_V = 14.5$ source, was used as adaptive optics guide star with the visible wavefront sensor. From narrowband observations of single stars throughout the night, the measured FWHM of point-like sources is about 0.″10, 0.″07, and 0.″08 at J, H, and K_s band, respectively. These images, similarly, have Strehl ratios of approximately 5%, 25%, and 40%.

We obtained deep images in which HV Tau AB is saturated, as well as shallow images with an additional neutral density filter and shorter exposures to record unsaturated images of the primary. Total integration times for the long exposures of 750 s, 480 s, and 165.5 s were recorded at J, H, and K_s, respectively, split in 8–20 dithered independent images. Total integration times for the shallow images were 100 s, 50 s, and 45 s, respectively, at J, H, and K_s. For each sequence of images, a sky was estimated by medianing all images, which was then subtracted from each image prior to cosmetic cleaning, which included bad pixels and cosmic ray correction, and flat-fielding. All resulting images were then shift-and-added to produce final images.

On 2002 November 26, we re-observed HV Tau with NAOS and CONICA using the 0.″0270 pixel scale, this time using the 1.″4 diameter coronagraph mask to block out the starlight from HV Tau AB and record deeper exposures on HV Tau C. Three 120 s K_s band images were recorded. A sky was subtracted off each image before they were cosmetically cleaned and flat-fielded. Finally, they were averaged to yield the final coronagraphic image. No point source is detected in the 30″ field

of view, preventing us from estimating the achieved FWHM and Strehl ratios.

2.1.2. 3–5 μm Imaging

On 2002 December 13, we observed HV Tau using the NIRC2 camera (P.I.: K. Matthews) installed behind the Keck II adaptive optics system (Wizinowich et al. 2000) to record images using the L' ($\lambda_0 = 3.78$ μm, $\Delta\lambda = 0.70$ μm) and M_s ($\lambda_0 = 4.67$ μm, $\Delta\lambda = 0.24$ μm) filters and the 0.″00996 plate scale (Ghez et al. 2008). HV Tau AB was used as a Natural Guide Star (NGS) for the adaptive optics system. To reduce thermal background and provide a more symmetric and smoother point-spread function (PSF), we used the "inscribed circle" pupil stop, resulting in an effective primary mirror diameter of 9 m. At L', four images, consisting of 300 coadded 0.181 s individual integrations each (for a total of 217.2 s on source integration), were acquired with the sources dithered on-chip between images. A fifth image was acquired with all stars moved out of the detector field of view (10″) to estimate the sky level. At M_s, 500 individual 0.150 s integrations were coadded using a reduced 6″ wide field of view, necessary to avoid background saturation on the intense thermal background. A total of 21 such images were obtained with the stars moved about in the available field of view, representing a total integration time of 1575 s. The corresponding sky was estimated by median-combining all frames.

On 2004 November 3, we re-observed HV Tau with NIRC2, this time using the newly available Laser Guide Star (LGS) module on the Keck II adaptive optics system (van Dam et al. 2006; Wizinowich et al. 2006). The laser system was run at 6 Watts output power, which produced a guide star with an equivalent magnitude of $m_V = 9.9$, and HV Tau AB was used as the tip/tilt correction point source. To take full advantage of the better image quality, the "largehex" pupil mask, which does not block any section of the primary mirror, was used throughout the observations. HV Tau was imaged in the L' filter with an 0.2 s integration coadded 100 times. This observing cycle was repeated 27 times, with the system alternatively located in opposite detector quadrants, providing a total integration time of 540 s. For each image, the subsequent one, with the star located in the opposite quadrant, was used as a sky frame.

All data sets were reduced using a similar strategy to that used in processing the NACO images (see also Duchêne et al. 2004). First of all, the sky thermal emission was subtracted. These subtracted images were then flat-fielded and had any bad pixels interpolated over. In the case of the LGS data set, a residual sky level in the frames was measured by taking the median value of the quadrants which do not have a star in the field. This value (typically corresponding to 0.05% of the initial sky value) was then subtracted off the cleaned images. All cleaned images in a given data set were then median-averaged. We measured FWHMs of 0.″09 and 0.″11 for point-like sources observed before/after HV Tau at L' and M_s for the NGS data set and 0.″08 at L' for the LGS data set. We estimated the corresponding Strehl ratios to be about 70% at L' (both in NGS and LGS modes) and 80% at M_s, using the "Strehl meter" tool developed by the Keck observatory.[11]

Given the high thermal background at L' and M_s, the resulting signal-to-noise on HV Tau C is limited, about 15, 20, and 5 in the peak pixel at L' (NGS, LGS) and M_s, respectively. To enhance detection without altering the intrinsic spatial resolution of the images, we smoothed them by using a running 2 pixel radius (≈0.″02) median-filtering circular mask, and rebinned them by a factor of 3 in both directions, resulting in an approximate final sampling of 0.″03 pixel^{-1} that still oversamples the resolution of the data sets.

2.2. Submillimeter and Millimeter Imaging

2.2.1. 1.3 and 2.8 mm Interferometric Imaging

On 2005 February 26, we observed HV Tau with IRAM's six-antenna Plateau de Bure Interferometer (PdBI; Guilloteau et al. 1992) in the 6Bp configuration, with baselines ranging from 71 m to 331 m. Simultaneous 110 GHz (2.76 mm) and 230.5 GHz (1.31 mm) observations of HV Tau were recorded in double-sideband mode with a bandpass of 640 MHz at each frequency. HV Tau was observed alternatively with phase calibrators 0415+379 and 0528+134 through an entire 11 hr transit, resulting in beam sizes of 1.″1 × 0.″9 (along position angle 38°) and 2.″1 × 1.″6 (along position angle 62°) at 1.3 and 2.8 mm, respectively. The average weather conditions resulted in rms phase noises on the order of 15°–40° at 2.8 mm and 8°–15° at 1.3 mm (using self-calibration from the 2.8 mm data), equivalent to an atmospheric "seeing" on the order of 0.″3 and 0.″6 at 1.3 and 2.8 mm, respectively. The absolute pointing uncertainty is on the order of 0.″1–0.″2. The quasars NRAO 150 and 3C 273 were used as absolute flux calibrators, resulting in a 10% uncertainty on all quoted fluxes. The data were reduced using the GILDAS package and selecting individual baseline visibilities for which the phase noise was less than 40° and flux variations were less than 20% based on calibrators measurements. Simultaneous observations of the ^{12}CO 2–1 transition (230.538 GHz rest frequency) with a 20 MHz bandpass were obtained to probe the gaseous component of the disk. Data reduction followed the same method as the continuum data, providing a three-dimension reconstructed datacube with a 0.1 km s^{-1} spectral resolution.

We obtained follow-up observations of HV Tau with the fifteen-antenna CARMA array in its C configuration, with baselines ranging from 24 to 300 m. On 2008 May 6 and 9, we tuned the receivers to a central frequency of 110 GHz (2.76 mm), while on 2008 May 29 we tuned them to 90 GHz (3.33 mm). The total continuum bandwidth is 2.8 GHz, split in 6 separate bands. Observing conditions were average and parts of the observations had to be flagged out because of poor phase coherence. Overall, the useful integration times on HV Tau were 3 hr 45 minutes at 110 GHz and 2 hr 30 minutes at 90 GHz. Observations of HV Tau were interleaved with pointings at 3C 111 and J 0530+135 which served as phase calibrators; flux calibration was performed by observing a planet (Uranus, Neptune) at the beginning of each track. The systematic uncertainty in CARMA's absolute flux scale is ∼20% (W. Kwon 2008, private communication). The data were reduced using the MIRIAD software package. The final 110 GHz map corresponds to the combination of both observing periods, and is characterized by a beam size of 1.″8 × 1.″4 (along position angle 116°); the 90 GHz map has a beam size of 3.″1 × 1.″7 (along position angle 124°).

2.2.2. 350 μm Single Dish Mapping

On 2008 January 28, we observed HV Tau at 350 μm with the 32 × 12 SHARC-II bolometer array (Dowell et al. 2003) installed at the Caltech Submillimeter Observatory. The array was scanned at an 8.″2 s^{-1} rate over a 60″× field centered on HV Tau. This scanning was repeated until a total integration of 600 s was achieved. Ceres and HL Tau, two secondary flux

[11] http://www2.keck.hawaii.edu/optics/aochar/Strehl_meter2.htm

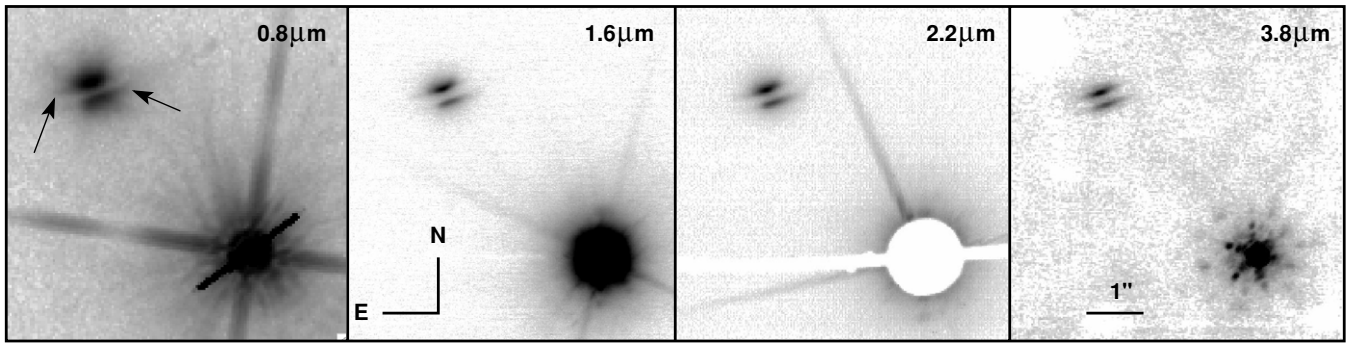

Figure 1. Scattered light images of HV Tau. The left most panel shows the F814W image obtained by Stapelfeldt et al. (2003) while the other three panels show our new images obtained at H and K_s with VLT/NACO (the K_s image is the coronagraphic one), and at L' with Keck/NIRC2 and the LGS adaptive optics system. The F814W image is shown on the logarithmic stretch to better highlight low-level features. The arrows point to the "rays" identified by Stapelfeldt et al. (2003). All other images are shown on a square root stretch. In all cases, the field of view is 6″ across. As discussed in the text, the L' image has been smoothed and resampled to improve the signal-to-noise ratio without degrading its spatial resolution.

calibrators, were observed immediately after with total integration times of 180 s and 300 s, respectively. The fluxes of both these sources are known to within 10%; their measured fluxes agreed to within this uncertainty. Conditions were excellent for submillimeter observations ($0.013 \leqslant \tau_{225\ \mathrm{GHz}} \leqslant 0.036$). All data were reduced using the CSO-developed CRUSH software, using a 6″ smoothing for HV Tau (a 4″ smoothing was used for the flux calibrators), to produce a final image that has an effective resolution of approximately 10″.

3. OBSERVATIONAL RESULTS

3.1. HV Tau as a Triple System

At all wavelengths, our adaptive optics images clearly reveal the typical morphology of HV Tau C as an opaque edge-on disk, namely two parallel, horizontal nebulae separated by a dark lane (Figure 1). They further show HV Tau AB to be systematically extended along the northwestern direction, although the pair is barely resolved due to its tight separation (see Figure 2). Here, we discuss the relative astrometry of all three components.

Focusing first on the wide pair HV Tau C–HV Tau AB, we estimate its separation and position angle based on the location of the centroid of both components. Despite saturation of HV Tau AB in some images, all images yield consistent estimates (see Table 1), with an average separation of 4.″04 ± 0.″02 and a position angle of 44.°6 ± 0.°6. There is marginal ($\approx 3\sigma$) evidence for a variation of the binary position angle as a function of wavelength, though this could be due to underestimated uncertainties on the absolute orientation of the detectors. We do not find any significant trend as a function of time at our level of precision. Based on the proper motion of HV Tau AB measured by Ducourant et al. (2005), the projected separation and position angle of the pair would have changed in the almost five years between the observations of Stapelfeldt et al. (2003) and ours by a total of 0.″12 and 2.°2, respectively, if HV Tau C had not been comoving with HV Tau AB. This can be rejected at the $\approx 5\sigma$ level in our data sets, and is further confirmed by the relative astrometry obtained at earlier epochs by Simon et al. (1992) and Woitas & Leinert (1998). We therefore conclude that HV Tau is a common proper motion pair with a projected separation of 565 AU, making it a bona fide triple system.

To obtain reliable relative photometry and astrometry for the tight HV Tau AB pair, we used PSF-fitting. We choose to analyze

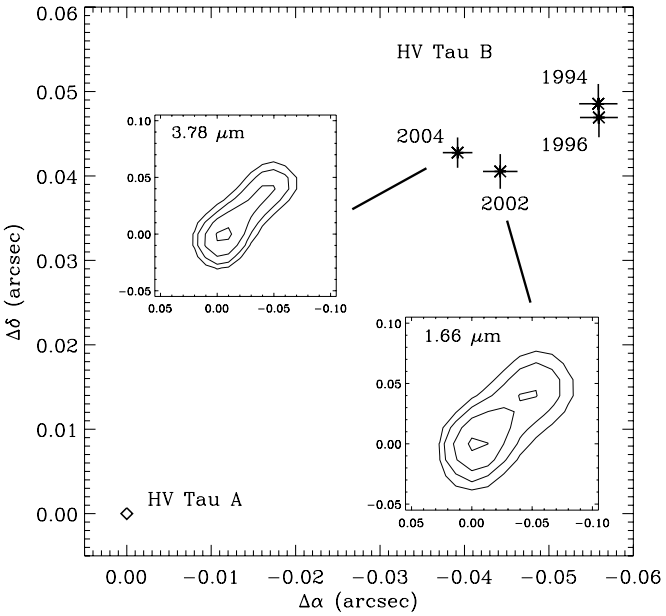

Figure 2. Orbital motion of HV Tau B with respect to HV Tau A, whose position is indicated by the diamond. The 1994 and 1996 points reflect astrometric measurements by Simon et al. (1996) and Monin & Bouvier (2000), whereas the other two points are our 2002 and 2004 measurements (see the text). The insets represent our H and L' images after a light Lucy deconvolution (25 and 50 iterations, respectively). While deconvolution better highlights the fact that the tight binary is resolved in our data, relative astrometry and photometry information for all our images was extracted by PSF-fitting of the original images.

the short H- and K_s-band VLT exposures and both L'-band Keck images, as they offer the best image quality and the most favorable ratio between binary separation and achieved resolution. For the VLT H-band and Keck L'-band images, we searched for adequate PSFs among images of single stars obtained on the same night as our HV Tau images. For the VLT K_s-band, we used a set of single stars from observations taken with the same set-up presented in Duchêne et al. (2007). PSF-fitting was performed using IRAF's *daophot* package. The resulting relative astrometry and photometry is listed in Table 1. The VLT and Keck NGS data have been taken within a few weeks of each other, and no measurable orbital motion is expected over such a short timescale. Averaging these three data sets, we find a separation of 0.″0595 ± 0.″0025 and a position an-

Table 1
Astrometric[a] and Photometric Properties of HV Tau

λ (μm)	Epoch	ρ_{AB-C} ($''$)	PA_{AB-C} ($^\circ$)	ρ_{A-B} ($''$)	PA_{A-B} ($^\circ$)	Δm_{A-B} (mag)
0.80	2000.19	4.04 ± 0.01	43.4 ± 0.3	...	...	...
1.27	2002.90	4.08 ± 0.03	43.5 ± 1.0	...	...	...
1.66	2002.90	4.06 ± 0.03	43.6 ± 1.0	0.054 ± 0.003	309 ± 3	0.88 ± 0.02
2.18	2002.90	4.03 ± 0.03	43.6 ± 1.0	0.062 ± 0.004	317 ± 2	0.88 ± 0.05
3.78	2002.95	4.03 ± 0.01	44.9 ± 0.1	0.063 ± 0.003	312 ± 2	0.53 ± 0.04
3.78	2004.84	4.02 ± 0.01	44.4 ± 0.1	0.058 ± 0.002	317.5 ± 1.5	0.59 ± 0.05
4.67	2002.95	4.07 ± 0.02	44.7 ± 0.2	...	...	...

Note.
[a] Astrometric uncertainties include both measurement (including centroiding) and absolute calibration uncertainties.

Table 2
Observed Properties of the HV Tau C Disk

λ (μm)	PA_{disk} ($^\circ$)	d_{neb} ($''$)	FR_{peak}	FR_{int}	$w_{5\sigma}$ ($''$)	Note
0.80	108.2 ± 1.2	0.335 ± 0.005	4.0 ± 0.2	2.8 ± 0.1	1.55 ± 0.03	
1.27	107.5 ± 1.1	0.281 ± 0.002	2.5 ± 0.2	2.4 ± 0.1	1.04 ± 0.07	
1.66	108.4 ± 0.9	0.284 ± 0.002	2.3 ± 0.2	2.2 ± 0.1	0.96 ± 0.05	
2.18	108.4 ± 0.7	0.275 ± 0.003	1.8 ± 0.1	1.80 ± 0.05	1.21 ± 0.07	Direct image
2.18	107.7 ± 0.8	0.267 ± 0.003	2.0 ± 0.1	1.82 ± 0.05	1.24 ± 0.07	Coronagraphic image
3.78	108.8 ± 1.3	0.237 ± 0.004	1.9 ± 0.2	1.8 ± 0.1	0.66 ± 0.03	NGS image
3.78	109.1 ± 0.9	0.236 ± 0.003	2.1 ± 0.2	1.5 ± 0.1	0.87 ± 0.05	LGS image
4.67	108.2 ± 1.7	0.231 ± 0.006	1.8 ± 0.3	2.3 ± 0.2	0.45 ± 0.05	

gle of $312.^\circ5 \pm 1.^\circ8$. The Keck LGS data, obtained two years later, yields a relative astrometry that is marginally consistent (2.5σ) with this estimate. The projected separation in our images appears to be 4σ–5σ smaller than earlier measurements (Simon et al. 1996; Monin & Bouvier 2000), but there is no significant change in position angle as a function of time (see Figure 2). This relative displacement is most likely due to orbital motion. The observed plane-of-the-sky velocity of HV Tau AB, $\approx$1.5 km s^{-1}, is roughly 1 order of magnitude too low considering the 10 AU projected separation of the binary compared to other T Tauri binaries (e.g., Ghez et al. 1995). The number of resolved measurements and the total amplitude in orbital motion are insufficient to attempt an orbital fit for HV Tau AB at this point. Nonetheless, the unexpectedly low measured orbital velocity suggests a highly elliptical orbit observed around apoastron passage, or a large out-of-the-plane separation which, combined with the nearly radial observed motion, would in turn imply that the orbital plane is almost perpendicular to the plane of the sky. Monitoring of the system in the next few years will help disentangle these two possibilities.

Our PSF fitting also yields relative photometry for the HV Tau AB binary. Considering the near-simultaneous H, K_s, and NGS L' images, we find evidence that HV Tau B is somewhat redder than HV Tau A in the near-infrared (see Table 1). In the framework in which none of the components possesses circumstellar material, this is an indication that HV Tau B is cooler than HV Tau A, consistent with it being fainter. Surprisingly, Simon et al. (1996) found a flux ratio in the visible that is closer to unity than our near-infrared measurements. Temporal variability of either component could be an explanation, although we note that both our L' flux ratios are consistent with one another despite being taken two years apart. Further monitoring is required to better understand the intrinsic colors of both components.

3.2. The HV Tau C Circumstellar Disk

3.2.1. Scattered Light Images

The near-infrared images presented here are of higher spatial resolution than those presented in Monin & Bouvier (2000) and Stapelfeldt et al. (2003), which both had a $0.''13$ resolution, and are comparable to the HKL' Subaru images of Terada et al. (2007). Our observations extend the wavelength coverage of HV Tau C to M_s for the first time and, combined with the *Hubble Space Telescope* (*HST*) F814W image of Stapelfeldt et al. (2003), offer an almost uniform spatial resolution ($0.''07$–$0.''11$, or 10–15 AU) view of the disk over the entire 0.8–4.7 μm range. This is critical to conduct unbiased studies of the wavelength dependence of the disk images.

To quantify the basic morphological properties of HV Tau C, we adopt the following method. At each wavelength, we first estimate the position angle of the dark lane, PA_{disk}, as the average of the position angles of each nebulae, as determined from fits of elliptical Gaussian intensity profiles. Averaging all estimates, we find a position angle of $108.^\circ3 \pm 0.^\circ4$, which we take as the orientation of disk midplane. The dark lane width, d_{neb}, is measured as the projection of the vector joining the light centroid of the two nebulae on the disk minor axis. Peak-to-peak flux ratios (FR_{peak}) are readily estimated, whereas integrated flux ratios (FR_{int}) are obtained by summing the flux within areas that encompass all pixels whose surface brightness is at least 5% (20% for the M_s image) of the peak surface brightness in the image. Finally, we measure the total extent of the disk along its major-axis, $w_{5\sigma}$, defined by the horizontal extent of the contour at the 5σ noise level. We note that the spherical halo identified by Stapelfeldt et al. (2003) dominates this measurement in the F814W image. All of these quantities are given in Table 2.

Several wavelength-dependent features can be noted in our images of HV Tau C. As Figure 3 illustrates, d_{neb} decreases by

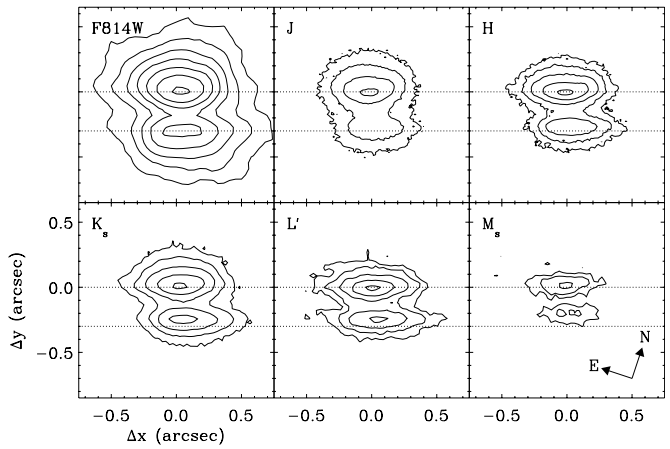

Figure 3. Contour plots of HV Tau C after rotating all frames to a common orientation where the disk midplane is horizontal. The K_s image is the VLT/NACO coronagraphic one and the L' image is the Keck/NIRC2 LGS image. The contours lie from 90% of the peak and by decreasing factors of 2 from there. The L' and M_s images have been smoothed to improve their sensitivity (see Section 2.1.2 for more details). The dashed lines are guidelines indicating the location of the peak of each nebula in the F814W image.

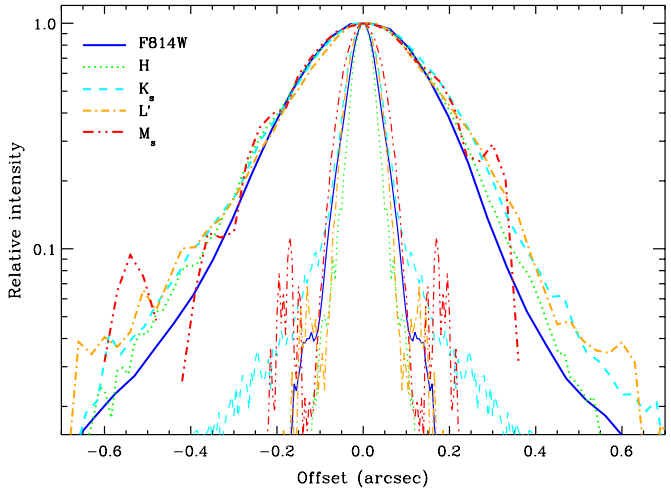

Figure 4. Lateral intensity profiles along the brightest (NE) nebula of HV Tau C. Profiles are drawn for the F814W (solid blue), H (dotted green), coronagraphic K_s (dashed cyan), LGS L' (dot-dashed orange), and M_s (triple-dot-dashed red) images of the disk. All profiles are drawn normalizing the peak intensity in each image to unity. The thin curves represent the azimuthally-averaged profile of the PSF corresponding to each observation, using the same linestyles and color coding. The nebula is well resolved and its intensity profile is remarkably constant across the wavelength range probed here.

(A color version of this figure is available in the online journal.)

about 30% from 0.8 to 4.7 μm. We further find that both FR_{peak} and FR_{int} smoothly decline toward longer wavelengths without ever reaching unity; rather, both flux ratios actually plateau longward of 2.2 μm. Finally, the intensity profile of the bright nebula along the disk major axis is remarkably invariant from 0.8 to 4.7 μm (see Figure 4). The measured FWHM is about 0.″35 at all wavelengths, i.e., a factor of 3–4 larger than the resolution of our images. This achromatic behavior is therefore not influenced by observational limitations but is rather intrinsic to the disk.

One main feature of the HV Tau C disk that was pointed out by Stapelfeldt et al. (2003) is the lateral asymmetry: the northeastern (bright) nebulae extends further on one side while the southwestern (faint) nebula extends further on the other side. This can be readily seen in Figure 3. In addition to this low-intensity asymmetry, the location of the nebulae centroids is also non-symmetric, suggesting a global asymmetry: the line joining the two centroids is misaligned by about 10° with respect to the disk symmetry axis as determined by the orientation of the dark lane. We do not find any significant variation of the asymmetry with wavelength nor time within our uncertainties.

Stapelfeldt et al. (2003) also discussed narrow structures, which they dubbed "rays," extending along the disk major axis beyond the main/bright nebula which they associate with the disk, with total extent up to 1.″4 in their optical images. We can track scattered light up similar distances at both K_s and L' in our images, a regime in which the halo is undetected. Although the exact nature of these features remains uncertain, this suggests that these "rays" trace the surface of the disk instead of being a mere shadow of the disk on the spherical halo. In that case, the actual disk size may be larger than the 50 AU assumed in the past.

3.2.2. Thermal Emission Regime

Both our PdBI and CARMA observations have a sufficient spatial resolution to disentangle the wide HV Tau pair. In all maps, a single source is detected, at the location of HV Tau C. HV Tau AB appears to have no significant emission at millimeter wavelengths with 3σ upper limits in our PdBI data of 6 mJy and 1.5 mJy at 1.3 and 2.8 mm, respectively.

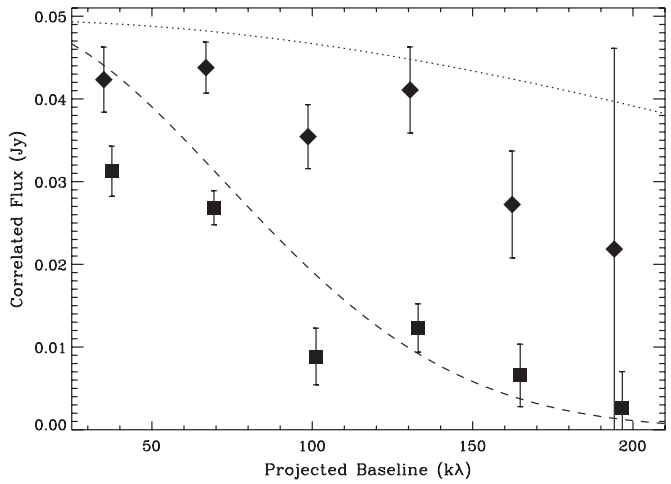

Figure 5. PdBI 1.3 mm correlated fluxes for HV Tau C as a function of projected baseline length for all baselines that are within 22.°5 of the disk major axis (squares) and within 22.°5 of its minor axis (diamonds). The major axis is assumed to be 108.°3 as determined from the scattered light images. The dashed and dotted curves represent the major- and minor-axis of the Gaussian fit to all visibilities, respectively, assuming a Gaussian 0.″3 atmospheric "seeing."

At 1.3 mm, HV Tau C is spatially resolved in our PdBI data, with a sharp decrease in correlated flux at the longest baselines along the position angle of the disk as defined from the scattered light images (see Figure 5). We therefore fit an elongated Gaussian profile to the visibilities, assuming that its minor axis is unresolved which is consistent with the data. This yields a total flux density of 49.5 ± 1.8 mJy, an FWHM of 1.″17 ± 0.″08 along the major axis, at P.A. 111° ± 3° east of north, in excellent agreement with the position angle derived from the scattered light images. This analytical fit is shown in Figure 5; deviations between observations and our simple fit result from the fact that the distribution of surface brightness in the disk is not a perfect Gaussian. The measured 1.3 mm flux agrees well with the previous single-dish measurement by

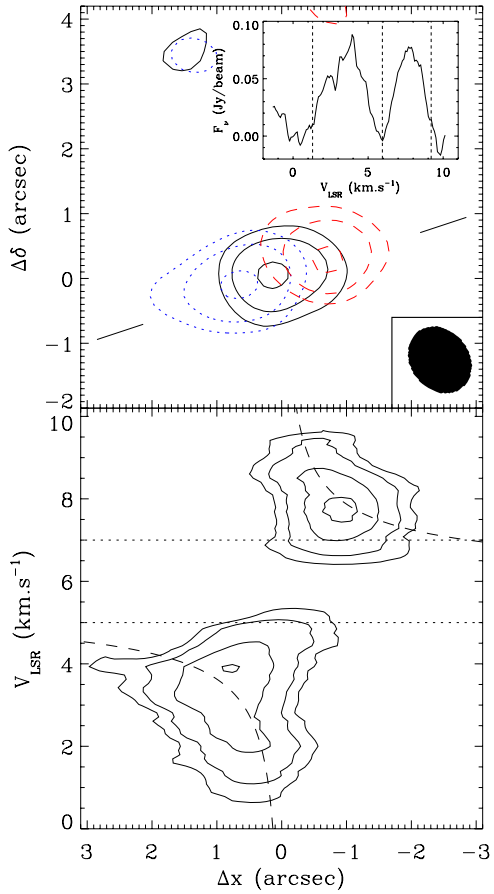

Figure 6. Top: contour plots of the blue (dotted contours, 0.8–6 km s^{-1} velocity range) and red (dashed contours, 6–9.5 km s^{-1} velocity range) parts of the ^{12}CO (2–1) line, superimposed on the contours of the adjacent 1.3 mm continuum (solid contours). Contours are drawn at 22.5%, 45%, and 90% of the peak intensity in each map. The reconstructed beam is shown for comparison. The origin of the relative coordinates is at $04^{h}38^{m}35\overset{s}{.}51$, $+26^{\circ}10'41\overset{''}{.}5$ (J2000), the nominal position of HV Tau C. The inset represents the integrated line profile. Bottom: position–velocity diagram along the disk major axis (indicated by the two solid segments in the top panel). The three-dimensional datacube has been smoothed using a 1 km s$^{-1}\times1''$ running boxcar function. The contours in the position–velocity diagram are at 15%, 30%, 60%, and 90% of the peak intensity. The dashed curve represents the theoretical Keplerian rotation curve for an 0.7 $M_{\odot}$ star with $v_{\rm sys}$ = 5.75 km s^{-1}. This is not meant as a fit but a reference to guide the eye. The dotted lines indicate the velocity range in which ^{13}CO emission from the Taurus molecular cloud was observed by Mizuno et al. (1995) at the location of HV Tau.

(A color version of this figure is available in the online journal.)

Beckwith et al. (1990). At 2.8 mm, the source is unresolved with the PdBI, with a flux density of 7.1 ± 0.5 mJy. The CARMA observations do not resolve the disk either, and we extracted point-source fluxes of 8.0 ± 2.1 mJy at 2.8 mm and 3.8 ± 0.9 mJy at 3.3 mm. Flux calibration uncertainties of 10% and 20% must be added for the PdBI and CARMA observations, respectively.

A single point-like source is detected in our 350 μm CSO map of HV Tau with a flux of 0.370 ± 0.030 Jy; a 10% uncertainty for flux calibration must be quadratically added. The resolution of this data set, roughly 10″, does not allow us to spatially resolve the wide pair. However, taking advantage of the strong detection of the system ($\approx20\sigma$), we use the nearly simultaneous observation of the bright source HL Tau with the same set-up to determine an accurate astrometric positioning (Mundy et al. 1996). The 350 μm source is found to be located at ($04^{h}38^{m}35\overset{s}{.}50$, $+26^{\circ}10'40\overset{''}{.}6$, J2000) with an uncertainty of

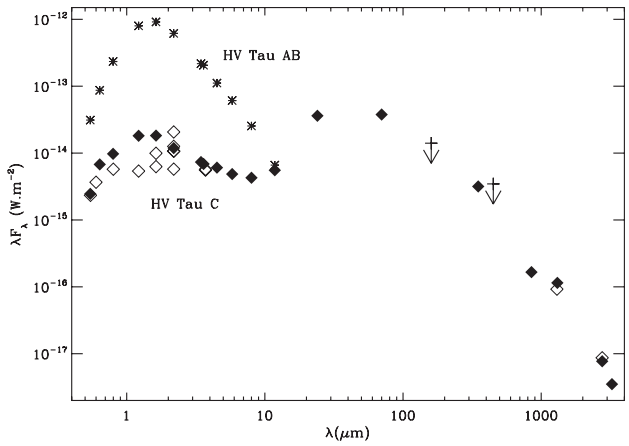

Figure 7. SED of HV Tau AB (asterisks) and HV Tau C (diamonds). Filled diamonds and upper limits indicate the photometry data set considered in our model fitting (see Table 3) whereas empty diamonds represent photometry at other epochs, illustrating in particular the optical and near-infrared variability of HV Tau C.

about 1″ in both directions. This is in excellent agreement both with the position of the lone millimeter source in our PdBI and CARMA maps and with the location of HV Tau C in optical and near-infrared images. We therefore conclude that HV Tau C is the dominant source of emission at 350 μm and assign all of the observed flux to that component.

3.2.3. Gas Emission

As shown in Figure 6, ^{12}CO 2–1 line emission is detected at the position of HV Tau C in our PdBI observations. The integrated spectrum shows two distinct peaks, with a near-zero trough separating them. The trough in the middle of the line is likely due to contamination by large-scale emission from the surrounding molecular cloud that is filtered out by the interferometer. Mizuno et al. (1995) detected ^{13}CO emission in the 5.5–7 km s^{-1} from the molecular cloud at the location of HV Tau, consistent with this interpretation. We further find that the blueshifted and redshifted parts of the line emission are spatially distinct and symmetric about the continuum peak. The two line emission peaks are separated by about 1″.5, or 200 AU, spatially and 4 km s^{-1} in velocity. Finally, we note that the CO emission appears to extend beyond both the millimeter continuum and the scattered light images, suggesting that there is more to the system than meets the eye in continuum data sets.

3.2.4. The SED of HV Tau C

To draw a complete picture of the HV Tau C disk, we compiled its SED by combining published fluxes with our new measurements. From the same references (see below), we also built the SED of HV Tau AB (Figure 7), which is well reproduced from the optical to the mid-infrared by a 3600 K, $\log g$ = 4.0, NextGen model from Baraffe et al. (1998) assuming $A_{\rm V}$ = 1.75 mag, in agreement with previous spectrophotometric estimates of the stellar properties of that component (Kenyon & Hartmann 1995; White & Ghez 2001).

Constructing the SED of HV Tau C is a delicate matter because of the large scatter in its published optical and near-infrared photometry (see also Monin & Bouvier 2000; Stapelfeldt et al. 2003). Figure 7 includes all published data and illustrates this variability. To construct a "representative" SED for HV Tau C, we elected to aim for smoothness. For instance, we adopt the most recent *KLN* photometry from

Table 3
Adopted SED for HV Tau C

λ (μm)	F_ν (mJy)	$\sigma(F_\nu)$ (mJy)	Date	Ref.	λ (μm)	F_ν (mJy)	$\sigma(F_\nu)$ (mJy)	Date	Ref.
0.545	0.446	0.097	1991 Jan–Feb	1	11.8	21.8	3.3	2002 Nov 13	3
0.638	1.44	0.31	1991 Jan–Feb	1	24	289	19	2005 Feb 28	5
0.797	2.59	0.42	1991 Jan–Feb	1	70	880	63	2005 Feb 28	5
1.22	7.38	0.97	1996 Aug 26	2	160	<750	···	2005 Feb 28	5
1.65	9.92	0.97	1996 Aug 26	2	350	370	30	2008 Jan 28	6
2.19	8.66	0.94	2001 Dec 1	3	450	<519	···	2000 Feb 2	7
3.45	8.44	0.37	2001 Dec 1	3	850	47	6	2000 Feb 2	7
3.6	8.25	1.25	2004 Mar 7	4	1300	40	6	1988 Apr 29–30	8
4.5	9.09	0.50	2004 Mar 7	4	2763	7.1	0.9	2005 Feb 26	6
5.8	9.39	0.51	2004 Mar 7	4	3252	3.8	1.2	2008 May 29	6
8	11.4	0.5	2004 Mar 7	4					

References. (1) Magazzu & Martin 1994; (2) Woitas & Leinert 1998; (3) McCabe et al. 2006; (4) Hartmann et al. 2005; (5) *Spitzer* Taurus Legacy Survey (Rebull et al. 2010); (6) This work; (7) Andrews & Williams 2005; (8) Beckwith et al. 1990.

McCabe et al. (2006), which matches well with the *Spitzer*/Infrared Array Camera (IRAC) data from Hartmann et al. (2005). We discard the *N* band measurements from Woitas & Leinert (1998) as they appear to overestimate the flux of both components by about 1 mag. Based on their agreement at the *K* band with the McCabe et al. photometry, we then adopted the *J H* fluxes from Woitas & Leinert (1998). Finally, we adopted the visible photometry from Magazzu & Martin (1994) which offers a smoother extension of the SED to short wavelengths than that of Stapelfeldt et al. (2003), although it was obtained almost a decade earlier. Apart from the *K*-band measurement by Simon et al. (1992), our selection is equivalent to consistently selecting the brightest measurement available at every wavelength. At longer wavelengths, we used the Multiband Imaging Photometer for *Spitzer* (MIPS) 24 μm and 70 μm detections and a 170 μm upper limit from the *Spitzer* Taurus Legacy Survey (Rebull et al. 2010). At 24 μm the astrometric accuracy is good enough to identify the detected source with HV Tau C with little or no contribution from HV Tau AB. In the longest wavelength regime, we adopt fluxes measured from our data and from Andrews & Williams (2005). The resulting SED, the most complete to date for an edge-on disk system, is shown as filled diamonds in Figure 7 and presented in Table 3.

The SED of HV Tau C can be characterized as a "double hump" (see Figure 7), which is typical of other edge-on disks (e.g., Strom & Strom 1994; Stapelfeldt & Moneti 1999; Wood et al. 2002). The short wavelength hump is dominated by photons emitted from the central star and the innermost region of the disk and scattered to the observer at the outer radius of the disk, whereas the long wavelength part represents the disk thermal emission propagated through the mostly optically thin disk to the observer. The wavelength of the turnover between the two humps is driven by the total column density of dust along the line of sight to the central star. We find this turnover to be between 8 and 11.8 μm although a more precise estimate would require analysis of a mid-infrared spectrum of the source. At longer wavelengths, Andrews & Williams (2005) noted that HV Tau C has an abnormally flat 850 μm to 1.3 mm slope. With our new observations, it appears that the 850 μm flux is indeed too low compared to the extrapolation from longer wavelength fluxes. Limiting our analysis to the 1.3–3.3 mm regime, we find a spectral index of $\alpha_{\rm mm} = 2.5 \pm 0.2$, where $F_\nu \propto \nu^{\alpha_{\rm mm}}$. This value is on the low end of the distribution observed for other protoplanetary disks (Beckwith & Sargent 1991; Mannings & Emerson 1994; Natta et al. 2007).

3.2.5. Qualitative Interpretation

Here we interpret some of the observational results listed above to make qualitative inferences about the HV Tau C system. We will then revisit in a quantitative way these conclusions on the basis of the radiative transfer modeling presented in Section 4.

The $\gtrsim$1 mag variability of HV Tau C in the near-infrared is larger than has been recorded for other T Tauri stars in the past (Eiroa et al. 2002; Alves de Oliveira & Casali 2008). It is therefore unlikely that this variability results from intrinsic fluctuations in the emission of the star and inner disk. A plausible alternative scenario could invoke a self-shadowing pattern in the disk that moves as a result of differential Keplerian rotation. In this framework, the structure responsible for the lateral asymmetry in the images would be located a few AU away from the central star to account for the absence of variability over the course of two years. This could be linked to the observed asymmetry in the scattered light images. Such a phenomenon has been documented in the HH 30 edge-on disk (Watson & Stapelfeldt 2007). One possibility is that the disk is warped as a consequence of the gravitational forces exerted by HV Tau AB.

The wavelength-dependent features of the scattered light images inform us about the absorption and scattering properties of the dust grains in the disk. For instance, the decreasing $d_{\rm neb}$ toward longer wavelengths is a consequence of the declining dust opacity (Stapelfeldt et al. 2003; Watson & Stapelfeldt 2004). The fact that the intensity profile along the bright nebula does not change with wavelength is suggestive of a dust population whose phase function is equally anisotropic at all wavelengths. A dust population similar to that of the interstellar medium, whose scattering asymmetry parameters drops rapidly beyond 1 μm (e.g., Weingartner & Draine 2001), seems inconsistent with our observations of HV Tau C. We note, however, that the flux ratio between the nebulae is not constant across the 0.8–4.7 μm range, even though it is also believed to be driven by the scattering asymmetry.

The slope of the SED of an edge-on disk between the near- and mid-infrared is a function of the disk geometry and of the grain size distribution and composition in the disk scattering surface. In their analysis of the "Flying Saucer" edge-on disk, Pontoppidan et al. (2007) concluded that the shallow 2–10 μm slope in that system implies the presence of a "significant amount of 5–10 μm grains" in that disk. Such grains are necessary to produce a high albedo in the

mid-infrared. While it is tempting to apply this argument to HV Tau C, uncertainties about the disk geometry prevents from reaching a firm conclusion just yet.

If the disk were optically thin to its own emission in the millimeter regime, the observed spectral index could be readily converted into an opacity power law index of 0.5 ± 0.2, characteristic of evolved dust grain populations that extend up to a few millimeter in size (Mannings & Emerson 1994; Natta et al. 2000; Andrews & Williams 2005). However, because the disk is very compact and viewed almost exactly edge-on, the optically thin assumption may be incorrect, so that grain growth cannot be claimed on this sole basis in this particular system. If the disk were indeed optically thick, one would expect the millimeter spectral index to steepen at longer wavelengths. We find $\alpha_{1.3-2.7\mathrm{mm}} = 2.5 \pm 0.2$ and $\alpha_{2.7-3.3\mathrm{mm}} = 3.4 \pm 0.6$, a difference that is not statistically significant. Flux measurements at even longer wavelengths are ultimately needed to conclude on this possibility.

In any case, there are several independent hints of the presence of grains at least a few microns in size, and maybe up to millimeter sizes, in the HV Tau C disk. However, none of these inferences are robust enough as they depend on some assumptions about the disk geometry, among other factors. The goal of the modeling presented in the next section is to simultaneously fit for the disk structure and the dust properties so as to solve for these ambiguities.

In the absence of a gas tracer whose emission from the cloud is negligible, we do not perform a complete Keplerian rotation analysis of our ^{12}CO observations. Qualitatively, *the measured amplitude of the velocity and positional offsets are consistent with a 0.5–1 $M_\odot$ central star* (see Figure 6). Observations in other molecular tracers are necessary to go beyond this simple analysis, however. We also note that the larger outer disk radius suggested by the gas emission is not a unique property of the HV Tau C disk. Indeed, this phenomenon is rather common among protoplanetary disks (e.g., Piétu et al. 2005; Isella et al. 2007; Panić et al. 2009), although few objects have been mapped at very high resolution in both the continuum and line emission. Hughes et al. (2008) have recently demonstrated that this can be reproduced if the surface density profile of disks is tapered, rather than sharply truncated, outside of a certain radius, for instance. Based on the gas emission alone, the disk outer radius might be as large as 100 AU, twice the estimate from the continuum and scattered light images. Since our entire analysis focuses on the dust component of the disk, we do not consider such large disk radii in our modeling.

4. PANCHROMATIC MODELING

The objective of this section is to compare our broad set of observations of HV Tau C to predictions of a radiative transfer code in order to constrain the main properties of the disk. Since this is the first attempt at simultaneously reproducing scattered light images, thermal emission maps, and the SED of HV Tau C, our approach consists in considering a simplified parameterized disk structure in an effort to search for a model that would represent a reasonable global fit to, rather than an exact representation of, all observations of this disk.

4.1. Radiative Transfer Models: Overall Framework

We use the MCFOST radiative transfer code (Pinte et al. 2006) which computes synthetic observables, such as SEDs and images, by propagating photon packets through the disk. Scattering, absorption, and re-emission by dust grains are taken into account following the Mie theory valid for homogeneous spherical grains. We assume that the dust grains are at the local thermal equilibrium with the surrounding radiation field throughout the disk. Synthetic temperature maps, SEDs, and images are computed simultaneously at all inclinations, allowing us to fit for that parameter as well. For each model, the temperature, SEDs, and images computation are performed using typically 1, 4, and 32 million packets, respectively. The disk is assumed to be passive, i.e., its only source of heating is radiation from the central star.

The disk geometry is described by its inner and outer radii, R_{in} (which we fix at 0.15 AU) and R_{out}, as well as by two independent power laws. The surface density profile of the disk follows $\Sigma(r) = \Sigma_0(r/r_0)^{\alpha}$. Vertically, we assume that $\rho(r, z) = \rho_0(r)\exp[-z^2/(2H(r)^2)]$, appropriate for a vertically isothermal, non-self-gravitating disk in hydrostatic equilibrium. Finally, we adopt a flaring law for the scale height, namely $H(r) = H_0(r/r_0)^{\beta}$. The dust content of the disk is characterized by a power-law size distribution, $dN(a) \propto a^{-p}da$ from a_{min} to a_{max}. We adopt the optical properties of the commonly used "astronomical silicate" mixture from Draine (2003) with $p = 3.7$ and $a_{\mathrm{min}} = 0.03$ μm. In all our models, we adopt a default distance of 140 pc, consistent with the system's parallax estimated by Bertout & Genova (2006). The central star is described by an effective temperature of 3800 K based on its spectral type (Woitas & Leinert 1998; White & Ghez 2001; Appenzeller et al. 2005), and we use the corresponding $\log g = 4.0$ NextGen synthetic spectrum (Baraffe et al. 1998). Although $R_\star$ is difficult to constrain in HV Tau C since we cannot measure the total bolometric luminosity of the object, we consider it as a free parameter since there is no simple method to fix it a priori.

Stapelfeldt et al. (2003) showed that adding an envelope to the system yields a much improved fit to the visible scattered light images of HV Tau C, especially to account for the roughly spherical halo that is detected well above the disk midplane. To implement this, we add a spherically symmetric envelope to our model, which is characterized by $R_{\mathrm{in}} = 1$ AU and $R_{\mathrm{out}} = 85$ AU (maximum extent of the "rays" identified by Stapelfeldt et al. 2003) to mimic the halo seen in the *HST* images. For this envelope, we use a total dust mass of 5×10^{-8} $M_\odot$, a radial density profile $\rho(r) \propto r^{-0.5}$ and interstellar-like dust grains ($a_{\mathrm{max}} = 1$ μm and $p = 3.7$). The optical depth through the envelope at $\lambda = 0.5$ μm is $\tau \approx 0.5$, i.e., the maximum acceptable considering the morphology of the visible images of the disk. While a spherical envelope has little physical relevance, as its free-fall time would be much shorter than the system age, we do not explore more sophisticated envelope models (e.g., rotation-supported). Indeed, we consider our approach as a reasonable "placeholder" to avoid systematically poor χ^2 values for our model scattered light images. Images of HV Tau C show that the envelope is only significantly detected shortward of 1 μm, anyway, and even then the region of highest signal-to-noise ratio, which contributes most to the total χ^2 is dominated by scattering off the disk. We therefore do not expect our simplistic parameterization to induce any strong bias on our results. Finally, we note that the asymmetry of the disk seen in scattered light image produces such strong deviations from our simple model that attempting to adjust the envelope profile is of little interest at this point.

Table 4
Model Parameters

Parameter	Min. Value	Max. Value	N_{sampl}	Sampling
Radiative Transfer Parameters				
M_{dust} ($M_\odot$)	10^{-5}	10^{-3}	5	Logarithmic
R_{in} (AU)	0.15		...	Fixed
R_{out} (AU)	50	75	2	Linear
H_0[a] (AU)	3	7	5	Linear
β	1.05	1.25	3	Linear
α	−1.5	0	4	Linear
a_{min} (μm)	0.03		...	Fixed
a_{max} (μm)	1	10^4	5	Logarithmic
p	3.7		...	Fixed
$R_\star(R_\odot)$	1.5	3	4	Linear
$T_\star$ (K)	3800		...	Fixed
i(°)	0	90	91	Linear in cos i
Post-processing Parameters				
D (pc)	140		...	Fixed
A_V (mag)	0	5	21	Linear

Note.
[a] H_0 is defined at a radius $r_0 = 50$ AU from the central star.

4.2. Parameter Space Exploration

4.2.1. Strategy and Modeling Grid

While we have set a number of parameters of the model, we still have to deal with an eight-dimensional parameter space: the total dust mass in the disk (M_{dust}), R_{out}, H_0 (defined at $r_0 = 50$ AU), β, α, a_{max}, $R_\star$, and the inclination to our line of sight (i, where $i = 0°$ corresponds to a face-on disk) are all free parameters. When computing synthetic SEDs, we also added a foreground extinction A_V following the interstellar extinction law which we considered as an additional free parameter, with values ranging from 0 to 5 mag. This extinction represents attenuation by material located around or between the HV Tau system and us and does not include attenuation by the edge-on disk and spherical envelope themselves.

For all model parameters except the inclination, we adopt a coarse sampling that encompasses reasonable estimates either from the previous modeling by Stapelfeldt et al. (2003) and Andrews & Williams (2005) or our own estimates above (see Table 4). For instance, we chose a range of values for a_{max} that extends from 1 μm to 1 cm. As shown in Figure 8, $a_{max} = 1$ μm results in an opacity law that is in reasonable agreement with the measured interstellar extinction law through the mid-infrared. By extension, we will refer to this model as "interstellar dust." The only parameter for which we use a large number of possible values is the inclination. MCFOST produces synthetic disk observables at all inclinations at once. The final images and SED are stored in several "inclination bins" that are equally spaced in cos i, appropriate for a random orientation prior. By using 91 independent inclination bins in all our simulations, we obtain a 0.°6 sampling in the vicinity of the perfectly edge-on geometry.

Exploring the parameter space with such a coarse sampling is computationally manageable, although it comes at the cost of failing to find a model that fits perfectly all data. Our original goal was to use this grid to identify a small region of the parameter space that produced a good fit to all observations and to run a second, finer grid in that smaller regions. However, as we discuss below, our analysis revealed that no single region of the parameter space could be selected that way, as different observations point toward different parts of the parameter space. We discuss possible avenues for improvement for future modeling efforts in Section 5. With eight free parameters in our model grid, we have computed over a million independent models, which required about 126,000 hr of CPU time on a 400 processor cluster, 92% of which was devoted to the synthetic SED calculation.

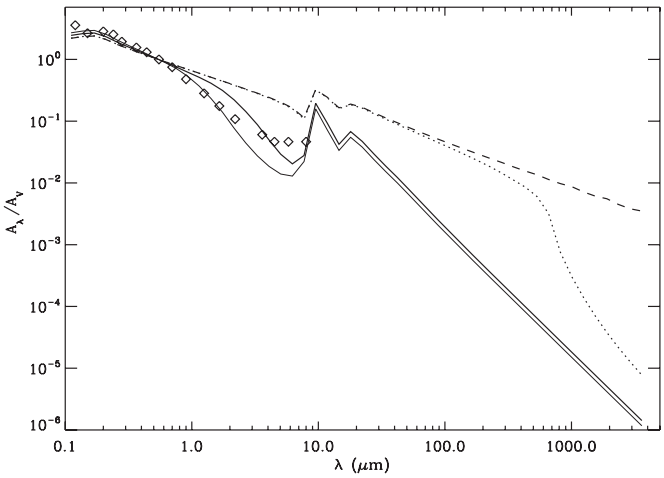

Figure 8. Extinction law for our dust models assuming $a_{max} = 1$ μm (thick solid), $a_{max} = 100$ μm (thick dotted), and $a_{max} = 1$ cm (thick dashed). Diamonds represent the measured extinction law from Cardelli et al. (1989) and Indebetouw et al. (2005). The thin solid curve represents a model with $a_{max} = 0.5$ μm (not used in our modeling) that best reproduces the measured interstellar extinction law up to 2 μm, but falls short of it in the 5–8 μm regime. The $a_{max} = 1$ μm is better in that regime and we use it as a proxy for "interstellar dust" in our model.

Because we chose a fixed value for R_{in}, the temperature at the inner edge of the disk varies from 800 to 1300 K in the grid. Similarly, the temperature at the outer edge ranges from 15 to 30 K. The radial dependence of the dust temperature in the midplane outside of ∼0.25 AU closely follows a power law, $T \propto r^{-q}$, whose index is in the range $q = 0.4$–0.6 and mostly depends on the amount of flaring in the disk. The dust

temperature at a given location depends primarily on $L_\star$, hence $R_\star$ and, to a lesser extent, on $a_{\rm max}$ (via the total dust opacity) and other geometric parameters. Our modeling strongly favors $R_\star = 3\ R_\odot$ (see below), for which the range in maximum temperature in the disk is 1100–1350 K, close to the sublimation temperature of dust grains. While setting $R_{\rm in}$ on the basis of this sublimation temperature for all models may be more physically relevant (Muzerolle et al. 2003), it is a computationally expensive iterative process, and we believe that it would not dramatically change our conclusions.

We decided to model five independent observables of HV Tau C, which we consider as representative of the entire data set available to us: its broadband SED (Table 3), the F814W, H and L' (LGS) scattered light images, and our IRAM 1.3 mm visibilities as a function of projected baselines. Our choice of wavelengths for the scattered light images to fit for is a trade-off between considering as wide a wavelength range as possible while securing data that have high enough spatial resolution and signal-to-noise per pixel. The latter criterion led us to discard our new $M_{\rm s}$ image in this modeling. In any case, a model that reproduces the F814W, H and L' images reasonably well is likely to also reproduce scattered light images at other wavelengths throughout the entire 0.8–5 μm range. MCFOST synthetic scattered light images were computed as monochromatic images at the effective central wavelength of each filter and with a 2″ total field of view. The thermal emission from both the disk and the envelope is neglected in computing these images, as most of the emission arises from the inner most regions, which is virtually unresolved as seen from the disk outer edge, where scattering toward the observer occurs. As discussed below, we only aim at reproducing the morphology and we have checked that this morphology is virtually unchanged if we take into account the disk emission, which otherwise induces a heavy computational cost. In the millimeter regime, we computed 1.3 mm thermal emission maps with a very fine spatial sampling to avoid aliasing in the Fourier transform (0.″05 pixel^{-1}).

4.2.2. Goodness-of-fit Estimates

While we are interested in finding the best possible model to account for the observations of HV Tau C, we also aim at determining the range of acceptable models around it. For this purpose, we adopt a Bayesian inference method (e.g., Lay et al. 1997; Akeson et al. 2002; Pinte et al. 2008), in which each model is assigned a probability that the data are drawn from the model parameters. In cases where the prior has a uniform probability distribution, as is the case here either on a linear, cosinus-like or logarithmic scale, this probability is $P = P_0 \exp(-\chi^2/2)$, where χ^2 is the reduced Chi square. The normalization constant, P_0, is chosen so that the sum of the probabilities over all models in the grid is unity. Once this is done for all models in our grid, we can derive the probability distribution for a given parameter by marginalizing the eight-dimensional probability hypercube against the other seven dimensions.

The computation of $\chi^2_{\rm SED}$ has 12 degrees of freedom. To take into account the noise intrinsic to Monte Carlo simulations, we ran 10 independent realizations of one of the best-fitting model and quadratically added the resulting standard deviation to the observational uncertainties. For the number of packets we used, this Monte Carlo noise is about 10% in the optical/near-infrared and (sub)millimeter regimes but reaches about 40% in the mid-infrared where photons have the hardest time escaping their deeply embedded emission region. Even though it is likely that this overestimates the uncertainties for non-edge-on models (for which photons escape more easily to the observer), it is of little importance since these models have very poor χ^2 values to start with, given that they do not produce the characteristic double-hump SED. In computing $\chi^2_{\rm SED}$, we chose to fit for $\ln(\nu F_\nu)$ instead of νF_ν, as this better handles the case of data sets that are dominated by calibration uncertainties (i.e., all measurements beyond 100 μm), which are multiplicative rather than additive in nature.

For scattered light images, we perform a pixel-by-pixel computation, though with a few adjustments. First of all, we resampled the H-band image to a pixel scale of 0.″027 for a higher signal-to-noise without compromising the spatial resolution. All synthetic images were then convolved with the same PSFs as used for the deconvolution of HV Tau AB (and a TINYTIM-generated F814W PSF[12]). We then aligned the model and empirical images using cross-correlation in the Fourier domain to determine the offsets with which the model images are best aligned with the observed ones. We further normalized all images to a peak value of unity since our goal is to reproduce the morphology of the images, the flux being fitted for in the SED. Finally, to avoid including many pixels where both the data and model are indistinguishable from zero and that would artificially improve our χ^2, we selected to use square binary masks encompassing the area where there is significant flux from HV Tau C. These masks are 2″, 1.″6, and 1.″4 on a side at F814W, H and L', respectively, resulting in 2017, 3713, and 2201 degrees of freedom. Tests conducted without these masks showed that this does not affect the ranking of the models from best to worse while ensuring that the best χ^2 are not artificially low, which would result in too relaxed constraints. Similar to the SED χ^2 computation, we estimated Monte Carlo noise maps by computing 10 realization of the best-fitting model at all three wavelengths. For the number of packets we used here, relative uncertainties range from less than 2% at the image peak to 8%–12% at the disk's outer edge.

At 1.3 mm, the available data are a series of correlated fluxes as a function of projected baselines. To reduce the number of visibilities to compute for each model and to improve their signal-to-noise ratio, we first flagged out all correlated fluxes whose uncertainty was larger than 0.1 Jy, i.e., twice the total flux from the source itself. We then averaged the correlated fluxes in the (u, v) plane using a 50 m bin size. This yields 60 independent measurements, or 52 degrees of freedom, at 1.3 mm. The model images were first rotated so that the disk midplane lies at a position angle of 108.°3, and convolved with a 0.″3 Gaussian "seeing." After padding the images with zeros to obtain the adequate total field of view, we computed their Fast Fourier Transform to obtain a set of synthetic correlated fluxes. As for the treatment of the scattered light described above, here we do not wish to fit for the total flux in the 1.3 mm map but for its morphology. Therefore, we convert the correlated fluxes into visibilities using the observed 49.5 mJy flux for the input data and the measured total flux in each map for the models. The 1.3 mm synthetic maps are essentially noiseless and we neglect the Monte Carlo noise in this regime.

4.3. Modeling Results

4.3.1. Best-fitting Models

The χ^2 values for the models that best fit each observation of HV Tau C are listed in Table 5. The combination of

[12] http://www.stsci.edu/software/tinytim/tinytim.html

Table 5
Goodness-of-fit Estimates for Selected Models

Model	χ^2_{F814W}	χ^2_H	$\chi^2_{L'}$	$\chi^2_{0.8-3.8\ \mu m}$	χ^2_{SED}	$\chi^2_{1.3mm}$	χ^2_{tot}
Best F814W model	**11.47**	9.24	17.69	38.40	139.89	15.30	193.59
Best H model	22.32	**3.74**	11.22	37.28	204.58	16.62	258.47
Best L' model	36.64	5.97	**3.84**	46.45	126.97	14.53	187.96
Best images model	16.39	5.17	5.80	**27.36**	174.95	15.87	218.17
Best SED model	68.10	34.30	42.45	144.85	**4.94**	16.10	165.89
Best 1.3 mm model	122.60	58.80	58.46	239.86	297.23	**9.19**	546.28
Best overall model	15.47	7.29	10.00	32.76	11.94	16.35	**61.04**

observational and numerical uncertainties used in computing the goodness-of-fit of a given model is unlikely to follow exactly a normal distribution. Caution should therefore be used when interpreting individual χ^2 values as they could be systematically biased. Nonetheless, the ranking of the models is likely correct and the model with the absolute lowest χ^2 value should be close to what would have been the best possible fit within the explored parameter space in the absence of non-Gaussian noise.

First of all, we note that the best reduced χ^2 for the SED, H- and L'-band images fit are in the 3.7–4.9 range. Considering the intrinsic asymmetry of the disk and the coarse sampling of the parameter space, we consider that these observations are well reproduced. While the intrinsic structure of protoplanetary disks is likely to be much more complex than the power law used here, the simplified parameterization adopted here appears reasonable and can therefore provide valuable insight about the disk properties. The fact that the best χ^2_{F814W} is only 11.5, i.e., much worse than the other two scattered light images, results in part from its higher signal-to-noise ratio which amplifies any departure from the models. In addition, the relative undersampling of the WFPC2 image results in a poorer ability to register images, thereby globally increasing all values of χ^2_{F814W}. Lastly, we note that the range of $\chi^2_{1.3mm}$ in our entire grid is very narrow, about a factor of 2 from best to worst, implying that this observation of HV Tau C is only mildly constraining for our model. This was to be expected considering that the disk is only marginally resolved in our PdBI data.

Figure 9 compares the observed SED of HV Tau C to several "best" models. The best overall model has a foreground extinction of $A_V = 1$ mag, marginally lower than the extinction we estimated for HV Tau AB. Both the models that best fit the F814W image and the best overall model with $a_{max} = 1\ \mu$m (i.e., interstellar-like dust) fail badly at reproducing the photometric data, with χ^2_{SED} of 139.9 and 20.7, respectively. Although these models produce a millimeter flux that is a factor of at least a few lower than the observed flux, it is interesting to note that they yield a shallow millimeter spectral index as a result of their high optical depth. Indeed, all models that adequately reproduce at least one of the HV Tau C observations have $\tau_{1.3mm} \gtrsim 15$ in the disk midplane. This is a clear reminder that millimeter spectral indices can be strongly affected by optical depth effects in the case of edge-on disks. Another shortcoming of an interstellar-like dust model, as discussed by Pontoppidan et al. (2007), is that it yields a near- to mid-infrared slope that is far too steep compared to observations if they are required to produce the right flux ratio between the two humps of the SED. This is a result of the vanishingly small mid-infrared albedo of any dust model that does not include grains of several microns in size. Therefore, the SED of HV Tau C points to the presence of at least intermediate-size grains in the disk.

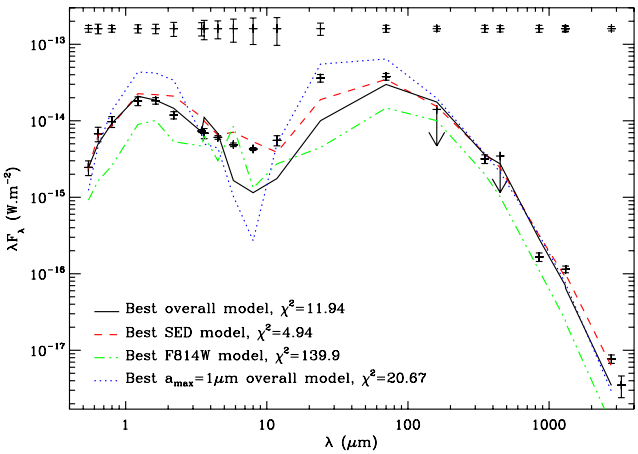

Figure 9. Comparison of the SED of HV Tau C (from Table 3, see also Figure 7) with various models: the best fit to all available data sets (black solid curve), the best fit to the SED alone (red dashed curve), the best fit to the F814W image (green dot-dashed curve), and the best overall fit with $a_{max} = 1\ \mu$m, i.e., interstellar-like dust properties (blue dotted curve). The thin error bars indicated at the top of the plot represent our Monte Carlo noise estimate. This noise is apparent in the jumps seen at 3 μm for the best overall model and at 6 μm for the best F814W fit.

(A color version of this figure is available in the online journal.)

Let us now consider the model scattered light images. Figure 10 compares the observed images to several key models. In addition to the factors listed above, the poorer fit to the F814W image likely arises from our simplistic treatment of the spherical halo, which is too bright at large distances above the disk midplane in the models. The models that best reproduce individual images each provide a good fit to the main features of the HV Tau C disk, such as the distance and flux ratio between the two nebulae. The model that offers the best trade-off between the three scattered light images nicely reproduces the wavelength dependency of d_{neb} but has roughly achromatic flux ratios between the nebulae. This is likely a consequence of the fact that this model, which has $a_{max} = 1$ cm, has an almost wavelength-independent scattering phase function, which is required to reproduce the intensity profiles shown in Figure 4. Interestingly, while the best model for each individual image corresponds to $R_{out} = 75$ AU, the best scattered light and best overall model both have an outer radius of 50 AU. Again, the disk asymmetry prevents us from unambiguously estimating the disk outer radius based on the images only. Finally, we note that the model that best fits the SED is a very poor fit to the scattered light images (χ^2 ranging from 34.3 to 68.1). The inclination of that model is 76.°3, giving the observer an almost grazing angle line of sight, resulting in a counternebula that is almost undetectable and an almost point-like appearance at L' which does not match the observed image at all.

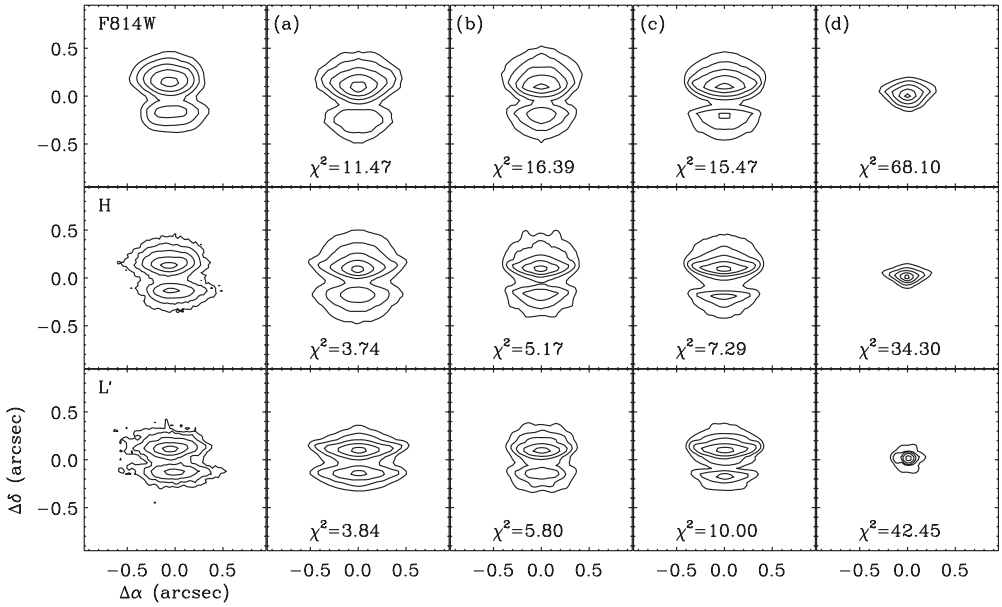

Figure 10. Contour plots of HV Tau C at 0.8 μm (top row), 1.6 μm (middle row), and 3.8 μm (bottom row). From left to right, the columns represent: the actual data, the best model in our grid at each wavelength (a), the best model to all three scattered light images simultaneously (b), the best overall model (c), and the best fit to the SED alone (d). All model images have been convolved with the appropriate PSF. In each plot, the contours lie at 80%, 40%, 20%, 10%, and 5% of the peak.

Although the 1.3 mm emission map is approximately reproduced by virtually all models in our grid, it is noteworthy that the best-fitting models have a face-on inclination. This stems from the fact that the disk, if viewed edge-on, is unresolved along its minor axis given the beam of our PdBI observations. However, our data show a slight drop of the correlated fluxes at the longest baselines along that position angle. Therefore, our modeling prefers a lower inclination in order to explain this feature. Since we know that the HV Tau C disk is indeed edge-on, this may indicate that the atmospheric phase noise increases with baseline in a way that differs from our Gaussian "seeing" approximation. Alternatively, it could be that the intrinsic thermal emission from the spherical envelope is stronger than in our model, which only contains small dust grains that are inefficient emitters at this regime. While this could in principle induce a bias in our modeling, we consider this effect as negligible considering that this data set is the least important in constraining the disk model.

4.3.2. Bayesian Analysis

Figure 11 shows the inferred probability distributions for each of our eight free parameters, after marginalization against all 7 other parameters. Fitting for each scattered light image separately yields probability distributions that are similar to each other and we only show the probability distribution for fitting all three images at once, for clarity purposes. The only differences between fits to individual images, associated with inclination and maximum grain size, are discussed below. The results from the fit to the F814W image tends to drive the results when grouping all three scattered light images because the other images are comparatively easier to reproduce, as shown by the lower best $\chi^2_{\rm H}$ and $\chi^2_{\rm L'}$ compared to the best $\chi^2_{\rm F814W}$.

We remind the reader that the derived probabilities that a given parameter takes a certain value are only valid within the framework of our modeling and are based on our approximate treatment of Monte Carlo noise in the simulations. Nonetheless, they represent a more reliable metric in our analysis than χ^2 values for individual models and they therefore better highlight how each observation informs our model of the disk. We note that the best individual model (shown as filled diamonds in Figure 11) has parameter values that correspond in most cases to the most likely value as determined from the Bayesian method, or to a value whose global probability is at least 20%. This demonstrates that noise in both data and model is well-behaved, providing support to the results of the Bayesian analysis.

The scattered light images place some constraints on $R_{\rm out}$, $a_{\rm max}$, i and, to a smaller extent, $M_{\rm dust}$. Since we have used flux-normalized images, $R_\star$ remains unconstrained. Similarly, α, β, and H_0 are not well constrained as a result of trade-off between these parameters and $M_{\rm dust}$. A scale height of 4–5 AU is preferred when fitting only the F814W but it is not conclusive and the other images have much flatter probability distributions for H_0. Our modeling of the scattered light images finds $R_{\rm out} = 50$ AU as the most likely value, although an outer radius of 75 AU cannot be formally excluded considering the disk asymmetry and total extent. The probability distribution for $M_{\rm dust}$ peaks at the lowest end of the range sampled here, and $P(M_{\rm dust} \leqslant 10^{-4}\,M_\odot) \approx 75\%$. It is worth noting that the probability distributions based on fitting each image individually are almost flat, but combining all three in a single fit yields a significant constraint as it helps solving for some of the ambiguities between parameters. Similarly, we find that $P(a_{\rm max} \leqslant 100\ \mu{\rm m}) \approx 90\%$ when fitting all three images at once, but there is an underlying trend as a function of wavelength. Indeed, $P(a_{\rm max} \leqslant 1\ \mu{\rm m})$ drops from 45% (most likely) at 0.8 μm, to 20% at 1.6 μm, and to 7% (least likely) at 3.8 μm, respectively. This gradual and smooth evolution with wavelength is probably indicative of a real physical phenomenon. Finally, the combined fit to the scattered light images suggests an inclination[13] of $82\overset{\circ}{.}7^{+0\overset{\circ}{.}6}_{-1\overset{\circ}{.}9}$. However, there is a marginal (2σ) trend as a function of wavelength: the most likely inclinations are $80\overset{\circ}{.}8^{+1\overset{\circ}{.}3}_{-1\overset{\circ}{.}9}$, $84\overset{\circ}{.}6\pm2\overset{\circ}{.}5$, and $85\overset{\circ}{.}9^{+1\overset{\circ}{.}3}_{-2\overset{\circ}{.}5}$ for the F814W, H, and L' images, respectively. This trend

[13] Uncertainty ranges are defined by the 34 percentile on each side of the most likely value.

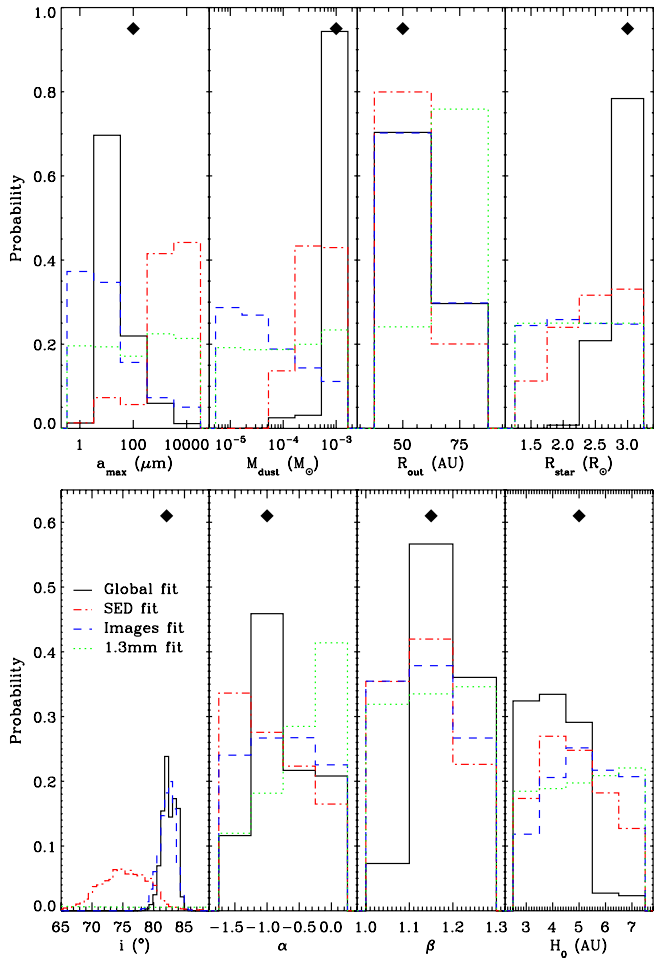

Figure 11. Bayesian inference probability distributions for the free parameters in our model, based on fitting the three scattered light images at once (dashed blue histograms), the SED (dot-dashed red), the spatially resolved 1.3 mm correlated fluxes (dotted green), and all observations at once (solid black). The probability distribution for the inclination based on the 1.3 mm is almost flat and very close to 0. For reference, the filled diamonds indicate the value of the parameters for the model with the absolute lowest $\chi^2_{\rm tot}$ in our grid. Note the different vertical scale in the two rows of plots.

(A color version of this figure is available in the online journal.)

stems from the inability of our model to produce a wavelength-dependent flux ratio between the nebulae without generating chromatic variations of the intensity profile along the major axis. This may indicate that our dust model does not possess the adequate chromatic behavior.

Considering now the SED, our modeling mostly provides constraints on the same parameters as the scattered light images. The SED fits favor the presence of large grains and a high total dust mass, with $P(a_{\rm max} > 100\ \mu{\rm m}) \approx 85\%$ and $P(M_{\rm dust} > 10^{-4}\ M_\odot) \approx 85\%$. Both conditions are necessary to produce sufficient fluxes at the long wavelength end of the SED. While interstellar-like grains can produce the observed spectral index, all models with such a dust population fall short in the 1–3 mm range by at least an order of magnitude. While SED fitting is generally not sensitive to the outer radius of a disk, here we find that a small outer radius is strongly preferred: $P(R_{\rm out} \leqslant 50\ {\rm AU})/P(R_{\rm out} \geqslant 75\ {\rm AU}) \approx 4$. This is because the relative height of the two humps in the SED and the depth of the trough that separates them is directly influenced by the disk geometry, via the total optical depths along our line of sight to the star on one hand and from the star to the upper layers of the outer disk on the other hand. Finally, the modeling of the SED yields a best fit inclination of $75\overset{\circ}{.}0^{+4\overset{\circ}{.}5}_{-3\overset{\circ}{.}9}$. The fact that the SED provides a weaker constraint on the disk inclination than the scattered light images is typical of all disk analyses. Nonetheless, the particular viewing angle of edge-on disk allows for a reasonably narrow range of inclination to be defined, and it is reassuring to note that the difference between the inclinations derived from the scattered light images and the SED is at the insignificant 1.6σ level.

The fit to the 1.3 mm yields much weaker constraints on the model parameters: all associated probability distributions are consistent with being flat except for $R_{\rm out}$, α and, to a smaller extent, i. As discussed above, this is a result of the fact that the disk is only marginally resolved in our PdBI data. To best reproduce the observed visibilities, the model favors a face-on geometry, a large outer radius and a flat surface density that places a lot of mass, hence of millimeter emission, at large radii. As far as inclination is concerned, the inferred most likely value is $0^{+50\circ}$, illustrating the weak preference for a face-on geometry. The constraints on both $R_{\rm out}$ and α are much stronger with a ratio of the most- to least-likely value of at least 4:1.

The strength of our modeling approach is to be able to fold all independent data sets in a single coherent fit, which both yields much sharper constraints and a view of the intrinsic contradictions between observations. For some parameters, such as β, H_0, and $R_\star$, the combined fit provides better constraints than any individual observation as a consequence of the fact that each observation is associated with a different set of ambiguities. We thus find that the disk is significantly flared ($\beta \gtrsim 1.15$), that its scale height at 50 AU is 5 AU at most, and that $R_\star \sim 3\ R_\odot$, which implies $L_\star \sim 1.7\ L_\odot$. Assuming that the accretion luminosity is negligible, this is consistent with a 1 Myr 0.7–1 $M_\odot$ central star (Baraffe et al. 1998), slightly larger than the mass estimated for HV Tau A (White & Ghez 2001). Although uncertainties are large, this is in rough agreement with the dynamical mass that we have estimated from the rotating CO disk.

In the case of $R_{\rm out}$ and α, the constraints set by the millimeter mapping are superseded by those from the scattered light images and the SED because the former is comparatively too easy to reproduce in our grid. While a $1/r$ surface density profile is preferred in our model, all other values tested in our grid have non-negligible probabilities. Similarly, our overall fit favors $R_{\rm out} = 50$ AU only by a factor of 2 over the larger radius. Excluding the 1.3 mm map from our analysis increases the preference for the smaller outer radius to a factor of 4:1, however. Future higher resolution millimeter observations are needed to better constrain both of these parameters. Also, the final probability distribution for the disk inclination is largely driven by the scattered light images. Our global fit suggests an inclination of $82\overset{\circ}{.}1^{+2\overset{\circ}{.}5}_{-1\overset{\circ}{.}9}$.

The most interesting results of our analysis concern $a_{\rm max}$ and $M_{\rm dust}$, for which scattered light images and SED lead to contradictory predictions (see Figure 11). The latter favors large grains and a high dust mass whereas the former suggests small grains and a low dust mass. Our global fit, which aims at finding the best possible trade-off between all constraints points to a very high dust mass ($M_{\rm dust} \geqslant 10^{-3}\ M_\odot$) and an intermediate maximum grain size ($a_{\rm max} \approx 10\ \mu$m). Since both of these values are essentially rejected ($P \lesssim 10\%$) by at least one of the observations, this "best" model should not be considered as a good fit. Rather, this apparent contradiction between the various

observations, which probably mirrors the trend in preferred $a_{\rm max}$ as a function of wavelength for the scattered light images, indicates that our model is too simplistic in at least some aspects. Possible explanations are explored in Section 5.

4.4. Comparison to Previous Modeling

There are three published models of the HV Tau C disk. In their discovery study, Monin & Bouvier (2000) derived a disk inclination of $\approx 84^\circ$ based on a single scattering model. That inclination has later been confirmed by subsequent models of the disk, including the present work. The second, most sophisticated to date, model of the disk was put forth by Stapelfeldt et al. (2003) who analyzed scattered light images at 0.8 and 2.2 μm. More recently, Andrews & Williams (2005) derived a total disk mass for HV Tau C based on its submillimeter flux although they did not conduct a complete SED fit for this source. Here we compare our model results to these previous efforts.

The model constructed by Stapelfeldt et al. (2003) was based on the same F814W image we have used here, and a lower quality 2.2 μm adaptive optics image that was characterized by a poorer resolution (0.″13 compared to 0.″08 for our VLT/NAOS image) and a smaller achieved Strehl ratio. Their conclusions are similar to ours in several ways. First of all, they found that it is easier to fit for the *K*-band image, as demonstrated by the lower achieved χ^2 value. Second, fitting for the envelope-free *K*-band image alone points toward an inclination that is closer to edge-on than if the F814W image is included in the fit. Conversely, when fitting both images simultaneously, they also note that they do not succeed in reproducing the wavelength dependence of the flux ratio between the nebulae.

If we temporarily focus on the F814W image alone, which is the most constraining data set in their fit, our Bayesian analysis yields $a_{\rm max} = 1$ μm, $M_{\rm dust} = 10^{-5}\,M_\odot$ and $H_0 = 4$ AU and $i = 80.^\circ8$. These values are consistent with those of Stapelfeldt et al. (2003) within our uncertainties. The derived inclination, somewhat further away from edge-on, may be explained by our different treatment of the spherical halo, which plays a non-negligible role in shaping up the morphology of HV Tau C at 0.8 μm. Finally, we note that our simultaneous fit to the F814W, *H*, and L' images favors $a_{\rm max} = 1$ μm. This model has a ratio of opacity of $\kappa_{0.8\,\mu{\rm m}}/\kappa_{2.2\,\mu{\rm m}} \approx 3.3$ and scattering asymmetry parameters of $g_{0.8\,\mu{\rm m}} = 0.6$ and $g_{2.2\,\mu{\rm m}} = 0.55$. These properties are very similar to those derived by Stapelfeldt et al. (2003), namely $\kappa_{0.8\,\mu{\rm m}}/\kappa_{2.2\,\mu{\rm m}} \approx 3.5$ and $g_{0.8\,\mu{\rm m}} = 0.65$.

Overall, we find that our fit to scattered light images is in good agreement with the previous modeling effort for this source, despite differences in strategy and parameter space covered. However, the models that best reproduce the F814W image produce millimeter fluxes that are 1–2 orders of magnitude too low in the millimeter regime, in apparent contradiction with the conclusion of Stapelfeldt et al. (2003), who found agreement within a factor of 2. The explanation for this discrepancy is that these authors assumed a ratio of dust opacity of $\kappa_{0.8\,\mu{\rm m}}/\kappa_{1.3\,{\rm mm}} = 6.10^3$. However, with our assumed dust composition, this ratio is about 7.10^4 for $a_{\rm max} = 1$ μm, accounting for most of the difference in predicted millimeter flux between the two models.

Andrews & Williams (2005) presented submillimeter observations of HV Tau C, which we have included in our fit. Because the source showed an unusual spectral index, they did not attempt to fit a full-fledged model but rather used an empirical recipe to convert the measured 850 μm flux into a disk mass. They derived $M_{\rm dust} = 2.10^{-5}\,M_\odot$, almost 2 orders of magnitude lower than the value we have derived here based on either the SED or global fit. The overall shape of the SED for HV Tau C suggests that the 850 μm flux is underestimated, possibly a factor of 3 or so, accounting for part of this discrepancy. In addition, the empirical law that Andrews & Williams (2005) used was mostly derived from sources which are not edge-on and for which optical depth effects are negligible. However, the model defined by the combination of each of the most likely parameter value has $\tau_{1.3\,{\rm mm}} \gtrsim 100$ in the disk midplane. We believe that this factor is the most important in explaining the difference in the disk masses inferred here and by Andrews & Williams (2005).

4.5. Shortcomings of the Model

While our model has been successful at reproducing the SED of HV Tau C, as well the morphology and several key chromatic behavior of its scattered light images, it falls short in several aspects which are worth exploring. As expected, a significant shortcoming of our model is its built-in axisymmetric assumption, which prevents us from finding perfect matches to any of the scattered light images. Since the nature of the asymmetry can only be speculated upon, no clear path to resolution can be provided until further monitoring clarifies its origin. This peculiarity is however not sufficient to account for the poor $\chi^2_{\rm tot}$ of our overall best-fitting model. The most glaring limitation of our model is the fact that it cannot account simultaneously for the SED on one hand and the scattered light images on the other. This fact, which most likely is independent of the axisymmetry of the model, implies that more complexity has to be included in the model.

The physical properties of dust grains are subject to improvement. Based on our modeling experience, the necessary requirements for an improved dust model in HV Tau C would be an interstellar-like opacity law and achromatic scattering phase function from 0.8 up to 5 μm and an optical-to-millimeter opacity ratio $\lesssim 10^4$. For one, one could devise a dust model that contains a fraction of C-rich grains to better conform to interstellar abundances. Departures from a simple power-law size distribution are also likely. Such a phenomenon has been observed in the interstellar medium (Kim et al. 1994; Weingartner & Draine 2001) and multi-modal distributions are predicted by dynamical models of grain growth, migration, and fragmentation in protoplanetary disks (e.g., Dullemond & Dominik 2005; Laibe et al. 2008; Zsom & Dullemond 2008). Another direction to explore is the possibility of non-spherical grains. Recently, Kimura et al. (2003) successfully reproduced the wavelength-independent anisotropic scattering observed in cometary dust by considering aggregates of small particles. Since the dust in HV Tau C also has achromatic scattering properties, aggregate grains are a candidate that deserves consideration in the future. In this context, it is interesting to note that fractal grains are expected to have a much flatter optical-to-millimeter opacity law (Wright 1987), akin to our models with $a_{\rm max} \geqslant 100$ μm, which are preferred in our analysis.

Since it appears difficult to simultaneously match all of these constraints with a single dust model, it will likely be necessary to drop the assumption that the dust properties are uniform throughout the disk. Since each type of observation probes a different region of the disk, *decoupling the dust properties in various regions of the disk would likely provide sufficient leeway.* In this picture, the disk would be quite massive and would contain large grains, up to millimeter-sized particles, in the midplane in order to explain the observed SED. However,

grains in the surface layers would not exceed a few microns in size to explain the scattered light images. To limit the number of free parameters, we have only considered fully mixed models here but we suggest that this hypothesis be further studied in future modeling of HV Tau C.

Future modeling efforts on HV Tau C should consider these various possibilities in improving on the model presented here. A robust strategy to move forward could consist in conducting detailed modeling of a particular type of observations, such as that conducted by Watson & Stapelfeldt (2004) on the scattered light images of HH 30 for instance. These specific analyses would allow one to extract the maximum amount of information from each observation and to feed it into a refined global model.

5. DISCUSSION

5.1. Global Properties of the HV Tau C Disk

Our objective in this work was to conduct the first "global" fit to the structure and dust content of the HV Tau C disk, one of the few objects in which such an effort is conducted in a self-coherent way. Although some uncertainty remains, our analysis has led to some robust conclusions about the HV Tau C disk. For instance, the total mass of the disk must be at the high end of the range probed here. Even in the presence of large grains, which are efficient emitters in the millimeter regime, the total dust mass has to be on the order of $M_{\rm disk} \sim 10^{-3}\,M_{\odot}$. Indeed, such a high dust mass is necessary to account for the observed fluxes and relatively high optical depths up to 3.3 mm. Assuming a canonical 100:1 gas-to-dust mass ratio, this implies that the disk is quite massive compared to the central star ($M_{\rm disk}/M_{\star} \gtrsim 0.1$). This is at the high end of the distribution observed for disks surrounding T Tauri stars (Andrews & Williams 2007). It is plausible that the disk is only marginally stable, in which case the presence of spiral density waves could be responsible for the observed asymmetry and/or variability of the system.

One respect in which the HV Tau C disk is special is its compact radius, a probable consequence of tidal forces induced by HV Tau AB. With $R_{\rm out} = 50$ AU and $\alpha = -1$, we derive a total surface density of 2800 g cm^{-2} 1 AU away from the star, comparable to the surface density inferred for the early Solar Nebula as well as for extra-solar planetary systems, albeit with a possibly flatter surface density profile (Hayashi 1981; Kuchner 2004). Indeed, the surface density at large radii in the disk, almost 60 g cm^{-2} at 50 AU, appears substantially higher than those derived for other protoplanetary disks (Dutrey et al. 1996; Kitamura et al. 2002). *The disk around HV Tau C is a clear example of the fact that binary systems can host circumstellar disks massive enough to form planets for timescales of several million years*. Indeed, HV Tau may well be a prototype for the earliest evolutionary stages of field stars that are found to host both an extrasolar planet and at least one stellar companion (e.g., Eggenberger et al. 2007; Mugrauer & Neuhäuser 2009).

As a test of the self-consistency of our model, it is interesting to compare the disk scale height we have derived, $H_0 \leqslant 5$ AU, to the simple assumption of vertical hydrostatic equilibrium that is embedded in our parametric disk structure. Assuming molecular hydrogen, the scale height can be written as $H_0^{\rm hydro} = 3.4(T/20\ {\rm K})^{1/2}(R/50\ {\rm AU})^{3/2}(M_{\star}/M_{\odot})^{-1/2}$ AU. Our best global model has a midplane temperature of 19 K at 50 AU, so that our upper limit on H_0 implies $M_{\star} \geqslant 0.44\,M_{\odot}$. This is not a stringent constraint on the mass of the central star, but we note that this lower limit violates neither the mass inferred from the spectral type and luminosity of HV Tau C nor the rough kinematic estimate we derived from the rotating CO disk. Both estimates are in the 0.7–1 $M_{\odot}$ range, for which the derived scale height would be 3.3–4 AU at 50 AU, which is consistent with our modeling. We therefore conclude that the outer disk can reasonably be described by a disk in hydrostatic equilibrium. In addition, *we suggest that HV Tau C may be the most massive component in the triple system.*

Finally, while large uncertainties remain regarding the dust properties, *it is clear that dust grains much larger than 1 μm are found in at least some parts of the disk*. This could be evidence for grain growth in the disk, although it is plausible that growth to a few microns may have predated the formation of the disk itself (McCabe et al. 2003). Indeed, analyses of extinction laws have already pointed to the presence of small quantities of grains a few microns in size in the interstellar medium and even more so in molecular clouds (Kim et al. 1994; Weingartner & Draine 2001; Indebetouw et al. 2005; Flaherty et al. 2007). On the other hand, growth to millimeter-sized grains, which seems supported by the analysis of the SED of HV Tau C, has most likely occurred in the disk itself. If the disk is indeed vertically stratified and no such grains are found in the disk surface, it remains unclear whether this is because of a very efficient settling process or a mere consequence of the difficulty to grow such large particles in the lower density regions of the disk.

5.2. Comparison to Other Circumstellar Disks

As outlined in the introduction, evidence for grain growth and dust stratification in protoplanetary disks has been mounting over the last two decades. It is therefore not surprising that our modeling of the HV Tau C disk calls for both processes. However, one must keep in mind that a given observation only probes a limited region of the disk. For instance, mid-infrared emission is dominated by emission from the inner few AUs at most, providing no information on dust stratification in the outer disk. In addition, there is an intrinsic observational bias in all studies whereby only a small range of grain sizes, those with the largest effective cross-section, actually contribute to the observed fluxes. Therefore, longer wavelength observations tend to systematically call for larger grain sizes, even if one limits the analysis to scattered light images (e.g., McCabe et al. 2003). Similarly, the mid-infrared silicate features arise from micronic and submicronic grains, providing no constraint on much larger particles. To draw a *complete* picture of dust properties throughout a given disk, it is therefore necessary to gather wide and homogeneous data sets, as we have done here.

As we have already mentioned, few objects have been studied in as much detail as our present analysis of HV Tau C. A clear dichotomy in terms of grain size was also found in the case of IRAS 04302+2247 (Wolf et al. 2003) but the interstellar-like dust grains favored by the scattered light images were located in the relatively massive envelope surrounding this embedded object and not in the disk itself. Vertical stratification was demonstrated in the massive GG Tau ring (Duchêne et al. 2004), although the available evidence only applies to grain smaller than 10 μm. The HK Tau B edge-on disk also appears to have a vertically stratified structure (Duchêne et al. 2003), although a self-consistent modeling of its SED, thermal emission maps and scattered light images is still required to make direct comparison with HV Tau C. On the other hand, Glauser et al. (2008) were able to reproduce a wide range of observations of IRAS 04158+2805 without the need to include vertical stratification. A similar conclusion was recently reached by Sauter et al. (2009) for CB 26. Overall, these detailed analyses

confirm the general trends outlined above that both grain growth and stratification are common, but not ubiquitous, in protoplanetary disks. They further offer the unique opportunity to test the detailed physics of dust evolution, such as the amount of dust stratification or its radial dependency (e.g., Pinte et al. 2007).

An interesting head-to-head comparison can be drawn between HV Tau C and IM Lup, for which Pinte et al. (2008) recently conducted a similar panchromatic modeling analysis, including scattered light images, millimeter emission maps, and the system's SED. The central stars have the same spectral type, and similarly high disk masses were inferred, making these two systems very similar. Contrary to the conclusion reached here however, Pinte et al. (2008) were able to place stringent constraints on all disk parameters and one may wonder what the reasons for this difference are. For one, the IM Lup disk is not seen edge-on, which allows the authors to fix some of the model parameters (e.g., $R_\star$, dust composition, M_d) in an unambiguous way. The smaller dimensionality of the parameter space to explore allowed Pinte et al. (2008) to sample it more finely. Another key feature of the IM Lup disk is that it is much less compact than HV Tau C and is well resolved at millimeter wavelengths, providing more stringent constraints on the model. Last but not least, a qualitative analysis of the SED of IM Lup readily demonstrated the need for a stratified structure in the disk, which introduces an extra degree of freedom that we could not afford in our analysis of HV Tau C. Nonetheless, our study has shown that *significant constraints on the disk properties can be obtained in an edge-on geometry*. No global modeling of HH 30, HK Tau B, or other prototypical edge-on disks, are yet available, but conducting such efforts should yield some interesting results and are needed to move forward in our understanding of protoplanetary disks.

6. CONCLUSION

We have obtained new 1–5 μm adaptive optics images of the HV Tau triple system at the VLT and Keck observatories, including the first 4.8 μm scattered light image of the edge-on HV Tau C disk. All of our images reveal a steady lateral asymmetry in the disk that indicates a departure from pure axisymmetry in the disk. This could be related to the known variability of HV Tau C. We extract precise relative astrometry from our new images and find that HV Tau AB–C constitutes a common proper motion pair. We also resolved the tight binary system HV Tau AB and found a surprisingly slow orbital motion compared to its projected separation, probably due to orbit eccentricity and/or a large deprojected physical separation. We have also obtained the first spatially resolved 1.3 mm continuum and ^{12}CO 2–1 millimeter maps of the HV Tau C disk with IRAM's PdBI interferometer. The continuum emission is resolved along the same position angle as the scattered light images, as expected from dust thermal emission. The CO map shows evidence of Keplerian rotation about an 0.5–1 $M_\odot$ central star. We also completed the SED of that component with new *Spitzer*/MIPS 24, 70, and 160 μm observations as well as observations at 350 μm, 2.8, and 3.3 mm at the CSO, PdBI, and CARMA facilities. The 1–3 mm spectral index of HV Tau C is relatively flat ($\alpha_{\rm mm} = 2.5 \pm 0.2$), indicative of the presence of millimeter-sized grains in the disk and/or high optical depth even at millimeter wavelengths.

To interpret these data along with previously published *HST* images of HV Tau C, we have computed a grid of radiative transfer models that produced synthetic disk observations. While we can reproduce most observational properties of HV Tau C, a Bayesian analysis of our model grid reveals that the SED and scattered light images of HV Tau C provide mutually exclusive constraints. As found previously, the scattered light images are best fit with a relatively small total mass and interstellar-like dust properties. Fitting the SED, however, requires almost 2 orders of magnitude more mass as well as a grain size distribution that extends to millimeter sizes. The mismatch between the two sets of constraints reveals an intrinsic shortcoming of our parameterized model, which assumes perfectly mixed dust. Indeed, the small maximum dust grain size inferred from fitting the scattered light images is impossible to reconcile with the long-wavelength end of the SED. In turn, this suggests that both grain growth and vertical stratification are present in the HV Tau C disk. While these phenomena have been suggested for other protoplanetary disks in the past, HV Tau C is one of a handful of objects that have been studied in sufficient details to eventually provide a complete picture of these processes.

Future observations of HV Tau C can help refine the model proposed here. For instance, high-resolution (0.″2 or better) millimeter mapping of the disk would better resolve it and provide more stringent constraints. In particular, obtaining observations at even longer wavelengths, 7 mm or 1.3 cm, would probe a regime in which the optical depth through the disk is much smaller and enable a more direct interpretation in terms of disk properties. On the longer run, mapping of the disk with ALMA in the submillimeter regime and in scattered light at 8–10 μm with the next generation of large ground-based telescopes will help bridge the gap between the scattering and thermal emission regimes at a roughly constant spatial resolution. In particular, very high resolution maps with ALMA may resolve this and other disks along the vertical axis, in order to probe their vertical stratification and, ultimately, to outline an evolutionary sequence.

We are indebted to all members of the GEODE group for many fruitful discussions about modeling of edge-on protoplanetary disks, and in particular to Marshall Perrin for developing some of the model analysis tools used in this project. We are grateful to Darren Dowell for his help with the astrometric calibration of our CSO data and to the CARMA staff for conducting the observations presented in this paper. The work presented here has been funded in part by National Science Foundation Science and Technology Center for Adaptive Optics, managed by the University of California at Santa Cruz under cooperative agreement No. AST-9876783, by the Programme National de Physique Stellaire of CNRS/INSU (France), and by the Agence Nationale de la Recherche through contract ANR-07-BLAN-0221. C.P. acknowledges the funding from the European Commission's Seventh Framework Program as a Marie Curie Intra-European Fellow (PIEF-GA-2008-220891). The authors acknowledge the contribution from Intel Corporation, Hewlett-Packard Corporation, IBM Corporation, and the National Science Foundation grant EIA-0303575 in making hardware and software available for the CITRIS Cluster which was used in producing some of the model computations presented in this paper. Support for CARMA construction was derived from the Gordon and Betty Moore Foundation, the Kenneth T. and Eileen L. Norris Foundation, the Associates of the California Institute of Technology, the states of California, Illinois, and Maryland, and the National Science Foundation. Ongoing CARMA development and operations are supported by the National Science Foundation under a cooperative agreement, and by the CARMA

partner universities. Some of the data presented herein were obtained at the W. M. Keck Observatory, which is operated as a scientific partnership among the California Institute of Technology, the University of California, and the National Aeronautics and Space Administration. The Observatory was made possible by the generous financial support of the W. M. Keck Foundation. The authors recognize and acknowledge the very significant cultural role and reverence that the summit of Mauna Kea has always had within the indigenous Hawaiian community. We are most fortunate to have the opportunity to conduct observations from this mountain.

Facilities: Keck: II, VLT:Yepun, IRAM:Interferometer, CARMA, CSO

REFERENCES

Akeson, R. L., Ciardi, D. R., van Belle, G. T., & Creech-Eakman, M. J. 2002, ApJ, 566, 1124
Alves de Oliveira, C., & Casali, M. 2008, A&A, 485, 155
Andrews, S. M., & Williams, J. P. 2005, ApJ, 631, 1134
Andrews, S. M., & Williams, J. P. 2007, ApJ, 659, 705
Appenzeller, I., Bertout, C., & Stahl, O. 2005, A&A, 434, 1005
Baraffe, I., Chabrier, G., Allard, F., & Hauschildt, P. H. 1998, A&A, 337, 403
Barrière-Fouchet, L., Gonzalez, J.-F., Murray, J. R., Humble, R. J., & Maddison, S. T. 2005, A&A, 443, 185
Beckwith, S. V. W., & Sargent, A. I. 1991, ApJ, 381, 250
Beckwith, S. V. W., Sargent, A. I., Chini, R. S., & Guesten, R. 1990, AJ, 99, 924
Bertout, C., Basri, G., & Bouvier, J. 1988, ApJ, 330, 350
Bertout, C., & Genova, F. 2006, A&A, 460, 499
Burrows, C. J., et al. 1996, ApJ, 473, 437
Cardelli, J. A., Clayton, G. C., & Mathis, J. S. 1989, ApJ, 345, 245
Chiang, E. I., Joung, M. K., Creech-Eakman, M. J., Qi, C., Kessler, J. E., Blake, G. A., & van Dishoeck, E. F. 2001, ApJ, 547, 1077
Cotera, A. S., et al. 2001, ApJ, 556, 958
D'Alessio, P., Calvet, N., & Hartmann, L. 2001, ApJ, 553, 321
D'Alessio, P., Calvet, N., Hartmann, L., Franco-Hernández, R., & Servín, H. 2006, ApJ, 638, 314
Dowell, C. D., et al. 2003, Proc. SPIE, 4855, 73
Draine, B. T. 2003, ApJ, 598, 1017
Duchêne, G., Bontemps, S., Bouvier, J., André, P., Djupvik, A. A., & Ghez, A. M. 2007, A&A, 476, 229
Duchêne, G., McCabe, C., Ghez, A. M., & Macintosh, B. A. 2004, ApJ, 606, 969
Duchêne, G., Ménard, F., Stapelfeldt, K., & Duvert, G. 2003, A&A, 400, 559
Ducourant, C., Teixeira, R., Périé, J. P., Lecampion, J. F., Guibert, J., & Sartori, M. J. 2005, A&A, 438, 769
Dullemond, C. P., & Dominik, C. 2004, A&A, 421, 1075
Dullemond, C. P., & Dominik, C. 2005, A&A, 434, 971
Dutrey, A., Guilloteau, S., Duvert, G., Prato, L., Simon, M., Schuster, K., & Menard, F. 1996, A&A, 309, 493
Eggenberger, A., Udry, S., Chauvin, G., Beuzit, J.-L., Lagrange, A.-M., Ségransan, D., & Mayor, M. 2007, A&A, 474, 273
Eiroa, C., et al. 2002, A&A, 384, 1038
Flaherty, K. M., Pipher, J. L., Megeath, S. T., Winston, E. M., Gutermuth, R. A., Muzerolle, J., Allen, L. E., & Fazio, G. G. 2007, ApJ, 663, 1069
Furlan, E., et al. 2006, ApJS, 165, 568
Ghez, A. M., Weinberger, A. J., Neugebauer, G., Matthews, K., & McCarthy, D. W., Jr. 1995, AJ, 110, 753
Ghez, A. M., et al. 2008, ApJ, 689, 1044
Glauser, A. M., Ménard, F., Pinte, C., Duchêne, G., Güdel, M., Monin, J.-L., & Padgett, D. L. 2008, A&A, 485, 531
Guilloteau, S., et al. 1992, A&A, 262, 624
Hartmann, L., Megeath, S. T., Allen, L., Luhman, K., Calvet, N., D'Alessio, P., Franco-Hernandez, R., & Fazio, G. 2005, ApJ, 629, 881
Hayashi, C. 1981, Prog. Theor. Phys. Suppl., 70, 35
Hughes, A. M., Wilner, D. J., Qi, C., & Hogerheijde, M. R. 2008, ApJ, 678, 1119
Indebetouw, R., et al. 2005, ApJ, 619, 931
Isella, A., Testi, L., Natta, A., Neri, R., Wilner, D., & Qi, C. 2007, A&A, 469, 213
Keene, J., & Masson, C. R. 1990, ApJ, 355, 635
Kenyon, S. J., & Hartmann, L. 1987, ApJ, 323, 714
Kenyon, S. J., & Hartmann, L. 1995, ApJS, 101, 117
Kessler-Silacci, J., et al. 2006, ApJ, 639, 275
Kim, S.-H., Martin, P. G., & Hendry, P. D. 1994, ApJ, 422, 164
Kimura, H., Kolokolova, L., & Mann, I. 2003, A&A, 407, L5
Kitamura, Y., Momose, M., Yokogawa, S., Kawabe, R., Tamura, M., & Ida, S. 2002, ApJ, 581, 357
Kuchner, M. J. 2004, ApJ, 612, 1147
Laibe, G., Gonzalez, J.-F., Fouchet, L., & Maddison, S. T. 2008, A&A, 487, 265
Lay, O. P., Carlstrom, J. E., & Hills, R. E. 1997, ApJ, 489, 917
Lay, O. P., Carlstrom, J. E., Hills, R. E., & Phillips, T. G. 1994, ApJ, 434, L75
Lenzen, R., et al. 2003, Proc. SPIE, 4841, 944
Magazzu, A., & Martin, E. L. 1994, A&A, 287, 571
Mannings, V., & Emerson, J. P. 1994, MNRAS, 267, 361
McCabe, C., Duchêne, G., & Ghez, A. M. 2003, ApJ, 588, L113
McCabe, C., Ghez, A. M., Prato, L., Duchêne, G., Fisher, R. S., & Telesco, C. 2006, ApJ, 636, 932
Mizuno, A., Onishi, T., Yonekura, Y., Nagahama, T., Ogawa, H., & Fukui, Y. 1995, ApJ, 445, L161
Monin, J.-L., & Bouvier, J. 2000, A&A, 356, L75
Mugrauer, M., & Neuhäuser, R. 2009, A&A, 494, 373
Mundy, L. G., et al. 1996, ApJ, 464, L169
Muzerolle, J., Calvet, N., Hartmann, L., & D'Alessio, P. 2003, ApJ, 597, L149
Natta, A., Grinin, V., & Mannings, V. 2000, in Protostars and Planets IV, ed. V. Mannings, A. P. Boss, & S. S. Russell (Tucson, AZ: Univ. Arizona Press), 559
Natta, A., Testi, L., Calvet, N., Henning, T., Waters, R., & Wilner, D. 2007, in Protostars and Planets V, ed. B. Reipurth, D. Jewitt, & K. Keil (Tucson, AZ: Univ. Arizona Press), 767
Panić, O., Hogerheijde, M. R., Wilner, D., & Qi, C. 2009, A&A, 501, 269
Piétu, V., Guilloteau, S., & Dutrey, A. 2005, A&A, 443, 945
Pinte, C., Fouchet, L., Ménard, F., Gonzalez, J.-F., & Duchêne, G. 2007, A&A, 469, 963
Pinte, C., Ménard, F., Duchêne, G., & Bastien, P. 2006, A&A, 459, 797
Pinte, C., et al. 2008, A&A, 489, 633
Pontoppidan, K. M., Stapelfeldt, K. R., Blake, G. A., van Dishoeck, E. F., & Dullemond, C. P. 2007, ApJ, 658, L111
Rebull, L. M., et al. 2010, ApJS, in press (arXiv:0911.3176)
Roddier, C., Roddier, F., Northcott, M. J., Graves, J. E., & Jim, K. 1996, ApJ, 463, 326
Rodmann, J., Henning, T., Chandler, C. J., Mundy, L. G., & Wilner, D. J. 2006, A&A, 446, 211
Rousset, G., et al. 2003, Proc. SPIE, 4839, 140
Sauter, J., et al. 2009, A&A, in press
Simon, M., Chen, W. P., Howell, R. R., Benson, J. A., & Slowik, D. 1992, ApJ, 384, 212
Simon, M., Holfeltz, S. T., & Taff, L. G. 1996, ApJ, 469, 890
Stapelfeldt, K. R., Krist, J. E., Menard, F., Bouvier, J., Padgett, D. L., & Burrows, C. J. 1998, ApJ, 502, L65
Stapelfeldt, K. R., Ménard, F., Watson, A. M., Krist, J. E., Dougados, C., Padgett, D. L., & Brandner, W. 2003, ApJ, 589, 410
Stapelfeldt, K., & Moneti, A. 1999, The Universe as Seen by ISO, ed. P. Cox & M. F. Kessler (ESA-SP 427; Noordwijk: ESA), 521
Strom, K. M., Newton, G., Strom, S. E., Seaman, R. L., Carrasco, L., Cruz-Gonzalez, I., Serrano, A., & Grasdalen, G. L. 1989, ApJS, 71, 183
Strom, K. M., & Strom, S. E. 1994, ApJ, 424, 237
Terada, H., Tokunaga, A. T., Kobayashi, N., Takato, N., Hayano, Y., & Takami, H. 2007, ApJ, 667, 303
van Dam, M. A., et al. 2006, PASP, 118, 310
Watson, A. M., & Stapelfeldt, K. R. 2004, ApJ, 602, 860
Watson, A. M., & Stapelfeldt, K. R. 2007, AJ, 133, 845
Watson, A. M., Stapelfeldt, K. R., Wood, K., & Ménard, F. 2007, in Protostars and Planets V, ed. B. Reipurth, D. Jewitt, & K. Keil (Tucson, AZ: Univ. Arizona Press), 523
Weidenschilling, S. J. 1997, Icarus, 127, 290
Weingartner, J. C., & Draine, B. T. 2001, ApJ, 548, 296
White, R. J., & Ghez, A. M. 2001, ApJ, 556, 265
Wizinowich, P., et al. 2000, PASP, 112, 315
Wizinowich, P. L., et al. 2006, PASP, 118, 297
Woitas, J., & Leinert, C. 1998, A&A, 338, 122
Wolf, S., Padgett, D. L., & Stapelfeldt, K. R. 2003, ApJ, 588, 373
Wood, K., Wolff, M. J., Bjorkman, J. E., & Whitney, B. 2002, ApJ, 564, 887
Wright, E. L. 1987, ApJ, 320, 818
Zsom, A., & Dullemond, C. P. 2008, A&A, 489, 931